https://doi.org/10.5194/egusphere-2026-3503
Preprint. Discussion started: 25 June 2026

A Multi-Angle and Polarization-Based Retrieval Algorithm for Aerosol Layer Height of Smoke and Dust

Pei Li[1], Yong Xue[1*], Davide Dionisi[2], Huihui Li[3], Shuhui Wu[4], Xingxing Jiang[5, 6], Botao He[1], Peng Wang[1], Liying Han[1]

[1]School of Environment and Spatial Informatics, China University of Mining and Technology, Xuzhou, 221116, China
[2]Institute of Marine Sciences (ISMAR), Italian National Research Council (CNR), Rome - Tor Vergata, Italy
[3]Zhejiang Academy of Emergency Management Science, Hangzhou, 310000, China
[4]Yunlong Lake Laboratory of Deep Underground Science and Engineering, Xuzhou, Jiangsu province, 221100, China
[5]Anhui Province Key Laboratory of Atmospheric Science and Satellite Remote Sensing, Anhui Institute of Meteorological Sciences, Hefei 230031, China.
[6]Shouxian National Climatology Observatory, Huaihe River Basin Typical Farm Eco–meteorological Experiment Field of CMA, Shouxian 232200, China.

Correspondence to: Yong Xue (yxue@cumt.edu.cn)

Abstract. The vertical distribution of aerosols governs their interactions with solar radiation and clouds, making it a key factor in their climatic and environmental effects. Existing passive methods for retrieving aerosol layer height (ALH) largely rely on a single observational dimension, such as spectral or multi-angle information, which provides limited constraints under complex aerosol conditions. To address this, we extend conventional spectral approaches by incorporating multi-angle polarimetric observations. Leveraging the high sensitivity of polarization signals to differences between molecular Rayleigh and aerosol scattering, along with broader scattering angle sampling, sensitivity to aerosol vertical structure is significantly enhanced. Using a vector radiative transfer model and information content analysis, we evaluate the contributions of multi-angle and polarimetric information to ALH retrieval. Results show that, compared with radiance-only observations, multi-angle polarimetric measurements substantially increase the degrees of freedom for signal, thereby improving ALH accuracy. An optimal estimation method is developed using HARP2 multi-angle polarimetric observations aboard PACE. Retrieved ALH values are validated against ATLID lidar observations on EarthCARE. For all collocated samples, HARP2 retrievals achieve a root mean square error (RMSE) of 1.03km, significantly lower than the 1.40km from TROPOMI, with a near-zero bias (−0.07km). For smoke, the RMSE is 1.12km, and for dust it further decreases to 0.92km. In a typical dust transport event, 84.5% of retrieval errors are smaller than 1km, highlighting the marked accuracy advantage of multi-angle polarimetric observations in ALH retrieval.

1 Introduction

Aerosol Layer Height (ALH) is a key parameter for characterizing aerosol radiative effects and climate feedback processes. The vertical distribution of aerosols directly influences their scattering and absorption of solar radiation through aerosol–radiation interactions (ARI). In addition, it exerts significant indirect climate effects by modulating cloud formation and

https://doi.org/10.5194/egusphere-2026-3503
Preprint. Discussion started: 25 June 2026

radiative properties via aerosol–cloud interactions (ACI) (Choi et al., 2021; Zeng et al., 2018). Consequently, reliance solely on column-integrated or horizontally distributed information is insufficient for accurately assessing aerosol-induced climate effects. Incorporating vertical structural information is therefore essential for improving the accuracy of radiative effect estimation. Beyond climate, ALH also significantly affects pollutant transport pathways and source attribution, and is thus of great importance in studies of air quality and health impacts (Gandham et al., 2022; Li et al., 2024; Parajuli et al., 2020).

Currently, the primary approaches for obtaining aerosol vertical structure information include active and passive remote sensing. Among active techniques, Lidar can accurately retrieve vertical profiles of atmospheric aerosols. For example, the Cloud-Aerosol Lidar with Orthogonal Polarization (CALIOP) onboard the CALIPSO (Cloud-Aerosol Lidar and Infrared Pathfinder Satellite Observation) satellite has provided long-term, continuous global observations of aerosol vertical distribution, as well as their optical and physical properties, with relatively high spatial resolution from June 2006 to August 2023 (Winker et al., 2007). As a member of the A-Train satellite constellation (Savtchenko et al., 2008), CALIPSO enables synergistic use with multi-source observational data, offering important support for aerosol studies and establishing the first long-term global dataset of aerosol and cloud profiles (Winker et al., 2010). However, its limitations are also evident. Due to its narrow swath, CALIOP provide only “curtain-like” vertical profile observations along the satellite track, making it difficult to achieve a complete three-dimensional characterization of aerosols. This limitation may lead to missed aerosol events and, to some extent, restricts its application in model validation and process studies (Cohen et al., 2018; Kahn et al., 2008; Liu et al., 2019; Zeng et al., 2020). As its successor, the EarthCARE (Earth Clouds, Aerosols and Radiation Explorer) satellite, launched on May 8, 2024, is now providing three-dimensional aerosol information (Illingworth et al., 2015). Nevertheless, achieving high spatial coverage and high-frequency three-dimensional characterization remains a key challenge that urgently needs to be addressed.

In contrast, passive remote sensing offers the advantage of wide-swath observations, enabling global-scale coverage with high spatial and temporal resolution, and providing an important data source for ALH retrieval. Passive remote sensing–based ALH retrieval methods can generally be classified into three categories: (1) stereo matching techniques based on multi-angle parallax; (2) spectral Retrieval methods based on radiative transfer theory; and (3) retrieval approaches based on polarization information. Among these, multi-angle stereo parallax methods estimate aerosol plume height by extracting geometric displacement through image matching at different viewing angles. The MISR (Multi-angle Imaging SpectroRadiometer) INteractive eXplorer (MINX) software system, developed by the NASA JPL (Jet Propulsion Laboratory) team based on MISR multi-angle observations, has been successfully applied to height retrieval of wildfire smoke plumes, volcanic ash, and dust aerosols (Diner et al., 2008; Nelson et al., 2008).

Another important technical approach is the use of multispectral observations from passive sensors, which is currently the most widely applied method. Representative techniques are based on the absorption features of molecular oxygen (O_2) in the A band (755–775 nm) and B band (685–695 nm). The underlying physical mechanism is that the presence of an aerosol layer modifies photon scattering paths (Xu et al., 2019). Specifically, more photons are scattered back to space at higher altitudes, thereby reducing their probability of penetrating into the lower atmosphere and being absorbed by O_2. As a result,

https://doi.org/10.5194/egusphere-2026-3503
Preprint. Discussion started: 25 June 2026

higher aerosol layers lead to stronger Top-of-Atmosphere (TOA) reflectance within the absorption bands. In practical applications, the Royal Netherlands Meteorological Institute (KNMI) has developed a neural network–based ALH retrieval algorithm using TROPOspheric Monitoring Instrument (TROPOMI) O_2A band observations. Results show that over ocean regions, the retrieved ALH exhibits a mean bias of approximately −1 km and a median difference of −0.76 km relative to reference data. However, over land, the retrieval bias increases significantly due to surface reflectance effects, with an average underestimation of about 2 km (Nanda et al., 2020). In addition, Xu et al. (2017) used TOA radiance observations from the O_2A/B bands of the EPIC satellite to achieve simultaneous retrieval of ALH and aerosol optical depth (AOD) over ocean regions. Building on this, Chen et al. (2021a) were the first to retrieve ALH using TROPOMI O_2 B band observations, further demonstrating the feasibility of this technical approach.

In addition to the visible–near-infrared bands, thermal infrared methods estimate ALH by exploiting the intrinsic thermal emission characteristics of the Earth–atmosphere system. It has shown that in the presence of dust aerosols, the TOA brightness temperature (BT) in the 8–12 μm atmospheric window region generally decreases and exhibits a negative spectral slope with respect to wavenumber around the 11 μm band. This spectral behaviour is highly sensitive to ALH and particle size distribution (Pierangelo et al., 2004; Sokolik, 2002). Therefore, by jointly utilizing information from multiple infrared window channels, it is possible to simultaneously retrieve AOD and ALH.

In comparison, near-ultraviolet remote sensing offers unique advantages for aerosol detection. Surface reflectance over land is generally low in this spectral range, which helps reduce interference from surface reflection (Dubovik and King, 2000; Li et al., 2025; Torres et al., 2002, 1998). In addition, near-ultraviolet observations are more sensitive to absorbing aerosols. Jeong and Hsu (2008) proposed an algorithm for retrieving aerosol single-scattering albedo (SSA) and layer height (Aerosol Single-scattering Albedo and Layer Height Estimation, ASHE) by synergistically using observations from the VIIRS and OMPS sensors. This method retrieves ALH and SSA by minimizing the residuals between measured ultraviolet radiance and simulated radiance under cloud-free and aerosol-free conditions. Subsequently, Lee et al. (2015) further extended this approach to dust aerosol scenarios.

Meanwhile, polarization observations provide an additional dimension of information for aerosol vertical structure retrieval. Using data from the Research Scanning Polarimeter (RSP), Wu et al. (2016) found that polarization signals in the near-ultraviolet and blue spectral bands exhibit strong sensitivity to ALH, highlighting the considerable potential of polarization measurements for characterizing aerosol vertical distribution.

In summary, existing passive remote sensing studies have explored ALH from multiple perspectives, including multi-angle, spectral, and polarization dimensions. However, early methods were often limited to a single observational dimension (e.g., spectral-only or angular-only), resulting in strong coupling effects among retrieval parameters — particularly the mutual constraint between ALH and AOD — which limits retrieval accuracy and robustness. With the advancement of next-generation satellite platforms integrating multi-angle, multispectral, and polarization sensors, the richness of observational information has been significantly enhanced, providing a solid foundation for synergistic multi-dimensional retrieval (Dubovik et al., 2019; Li et al., 2018; Mishchenko et al., 2007). Multi-angle observations strengthen the physical constraints

https://doi.org/10.5194/egusphere-2026-3503
Preprint. Discussion started: 25 June 2026

on atmospheric scattering geometry by capturing radiative characteristics over a wider range of scattering angles. Meanwhile, polarization measurements, with their high sensitivity to aerosol particle size, refractive index, and phase function, offer diagnostic information that is independent of radiance intensity (Dubovik et al., 2011). The integration of these complementary observations not only enhances the separability of retrieval parameters, but also provides new opportunities for more accurate characterization of aerosol vertical distribution (Hasekamp and Landgraf, 2007). Nevertheless, multi-angle polarization retrieval still faces challenges, including uncertainties in surface polarized reflectance models and errors in aerosol model assumptions. Moreover, the quantitative contributions of multi-dimensional observations to ALH retrieval have not yet been systematically assessed, highlighting the need for further investigation.

Motivated by the above considerations, the present study aims to enhance information content by extending ALH retrieval from a single spectral dimension to a multi-dimensional observational space that integrates spectral, angular, and polarization measurements. This approach provides stronger physical constraints for retrieving aerosol vertical structure from passive remote sensing. Through radiative transfer simulations and sensitivity analysis of the Stokes vector, the response of TOA polarized radiance to aerosol vertical distribution and scale height is systematically evaluated. The variation in information contribution under different viewing geometries is further investigated. Based on these analyses, a joint retrieval strategy is developed within an optimal estimation method to achieve robust ALH retrieval over both ocean and land surfaces.

The remainder of this paper is organized as follows. Section 2 introduces the satellite data used in this study. Section 3 presents the sensitivity and information content analysis of ALH based on information theory. Section 4 describes the multi-angle polarization retrieval method. Section 5 provides validation and analysis of the ALH retrieval results. Finally, Section 6 summarizes the main findings and discusses future perspectives.

2 Data Description

To support ALH retrieval based on multi-angle polarimetric observations and its accuracy evaluation, this study establishes an observation and validation framework using multi-source remote sensing datasets. The datasets used include multi-angle polarimetric measurements, aerosol column-integrated properties, surface reflectance auxiliary products, passive remote sensing ALH products, and active Lidar profile data. Specifically, the datasets comprise: (1) multi-angle polarimetric observations from the Plankton, Aerosol, Cloud, ocean Ecosystem satellite (PACE)/HARP2 (Hyper-Angular Rainbow Polarimeter-2); (2) AOD and surface reflectance products from the Suomi National Polar-orbiting Partnership (SNPP)/Visible Infrared Imaging Radiometer Suite (VIIRS); (3) ALH products from Sentinel-5P/TROPOMI; and (4) Lidar profile data from EarthCARE/ATLID (Atmospheric Lidar).

The local overpass times of PACE, SNPP, Sentinel-5P, and EarthCARE are approximately 13:00, 13:30, 13:30, and 14:00, respectively. Therefore, the temporal differences among HARP2 observations, TROPOMI ALH products, and

https://doi.org/10.5194/egusphere-2026-3503
Preprint. Discussion started: 25 June 2026

ATLID Lidar measurements are generally within about one hour. This relatively short time interval facilitates effective intercomparison and validation between ALH retrievals derived from multi-angle polarimetric observations and those obtained from independent active and passive satellite measurements.

2.1 HARP2

Multi-angle polarimetric observations are obtained from HARP2, which is onboard the PACE satellite (Xu et al., 2024). HARP2 provides ultra-multi-angle (up to over 60 viewing angles) and multispectral polarimetric measurements, delivering high-precision Stokes parameters in the visible and near-infrared bands (Werdell et al., 2019). Among these, the 441 nm channel exhibits high sensitivity to variations in ALH. Multi-angle polarization information enhances constraints on aerosol vertical distribution and microphysical properties, and significantly improves retrieval stability and information content compared with single-angle radiance observations. Based on this capability, this study develops a joint retrieval method using multi-angle I, Q, and U measurements from HARP2 to improve the sensitivity and accuracy of ALH retrieval.

This study uses the PACE_HARP2.L1C.V3.5km standard product with a spatial resolution of 3.5 km. The product has undergone radiometric calibration, geometric correction, and resampling, and provides multi-angle observations on a unified geographic grid (Gao et al., 2023). The datasets used in this study include: (1) solar zenith angle (SZA), viewing zenith angle (VZA), and relative azimuth angle (RAA), which characterize the observation geometry; (2) Stokes parameters I, Q, and U at 441 nm across 10 viewing angles, together with their corresponding uncertainty metrics (Istdev, Qstdev, and Ustdev). Here, I represents total radiance intensity, while Q and U denote the linear polarization components that characterize the polarization state of the scattering field. The associated standard deviations are used to quantify instrument noise and characterize error propagation in the retrieval process, providing a basis for subsequent uncertainty analysis.

2.2 VIIRS

This study incorporates aerosol product data from VIIRS onboard the SNPP satellite, specifically the AERDB_L2_VIIRS_SNPP dataset from the Level-2 Deep Blue aerosol product (NASA VIIRS Atmosphere Science Team, 2023). The following parameters were selected: (1) AOD at 550 nm as an indicator of column-integrated aerosol loading, with data pre-screened by an internal high-precision cloud masking algorithm (Hsu et al., 2013; Sayer et al., 2012); (2) surface reflectance at 488 nm to characterize surface reflection properties, providing auxiliary information for analysing land–atmosphere coupling effects; and (3) the Ångström exponent (AE) to facilitate AOD conversion across different wavelengths.

https://doi.org/10.5194/egusphere-2026-3503
Preprint. Discussion started: 25 June 2026

2.3 TROPOMI

The Level-2 ALH product (version 02.08.00) from the TROPOMI instrument onboard Sentinel-5P is used for validation (European Space Agency, 2021). In this version, surface albedo is incorporated into the optimal estimation state vector as a fitting parameter and is simultaneously retrieved together with ALH and AOD. This improvement enhances the consistency between radiative transfer simulations and observed spectra, and significantly reduces the impact of land–atmosphere coupling errors on the fitting of O_2 A band absorption features, thereby effectively mitigating the underestimation bias of ALH under high-reflectance surface conditions. Previous studies have shown that, compared with earlier versions, version 02.08.00 exhibits smaller systematic differences between land and ocean regions and achieves better agreement with active lidar observations (e.g., CALIOP and ATLID) (Graaf et al., 2025; Nanda et al., 2020, 2019).

In addition, the TROPOMI ALH product provides a continuous Quality Assurance (QA) metric ranging from 0 to 1, where 0 indicates retrieval failure or unreliable results, and 1 indicates fully successful retrieval. To ensure data quality, only pixels with QA$\geqslant$0.5 are retained for validation in this study, while those with QA<0.5 are considered unreliable and excluded. Furthermore, the ALH product has been cloud-screened using the VIIRS/SNPP Enterprise Cloud Mask (ECM), which further improves the reliability of the data.

2.4 ATLID

The reference data used for ALH validation are obtained from the ATLID active remote sensing instrument onboard the EarthCARE satellite, which was launched on May 28, 2024 (Illingworth et al., 2015). ATLID is an active sensor based on High-Spectral-Resolution Lidar (HSRL) technology, operating at a wavelength of 355 nm in the ultraviolet band. By separating molecular (Rayleigh) scattering from particulate (Mie) scattering signals, ATLID can independently retrieve aerosol and cloud backscatter coefficients, extinction coefficients, and polarization properties without requiring a priori assumptions of the lidar ratio (Nishizawa et al., 2026). Its native vertical resolution is approximately 103 m within the 0–20 km altitude range and about 500 m above 20 km. The along-track horizontal sampling interval is about 140 m, which is typically aggregated to an effective resolution of approximately 280–300 m in standard products (van Zadelhoff et al., 2023). This high vertical resolution makes ATLID particularly well suited for resolving the fine structure of aerosol layers and accurately determining layer top heights.

The specific datasets used in this study include the Level-2A products ECA_EXAF_ATL_AER_2A and ECA_EXAD_ATL_FM__2A. The former provides aerosol optical profile parameters, specifically the extinction coefficient at 355 nm, which can be used to derive aerosol layer centroid height or layer top height and serves as a reference for validating retrieval results. The latter includes the FeatureMask dataset, which contains a feature detection index ranging from 0 to 10, where 0 represents clear-sky conditions and 10 indicates a very high probability of optically thick clouds. This index is constructed based on probabilistic analysis of ATLID backscatter signals. It should be noted that this mask does not

https://doi.org/10.5194/egusphere-2026-3503
Preprint. Discussion started: 25 June 2026

distinguish between different particle types; instead, it is designed to differentiate strong signal regions, weak signal regions, and clear-sky areas, thereby facilitating the construction of vertical profiles for aerosol classification.

Owing to its high-precision vertical sensing capability and its physically based discrimination between aerosols and clouds, ATLID provides products with significant reference value for ALH validation. It offers an independent and reliable benchmark for evaluating ALH retrievals from passive remote sensing.

3 Sensitivity Analysis and Information Content of ALH

In ALH retrieval studies, the sensitivity of observations to target parameters and the information content contained in the observing system are key factors that determine retrieval accuracy and stability. Prior to the development of practical retrieval algorithms, it is necessary to systematically assess the retrievability of ALH under different observation conditions through radiative transfer forward simulations, thereby providing a theoretical basis for parameter selection, observation configuration design, and error control. Previous studies have shown that information content analysis and sensitivity assessment can effectively reveal the capability of an observing system to constrain atmospheric vertical structure parameters (Ding et al., 2016).

Therefore, this section constructs idealized observation scenarios based on a radiative transfer model. Under prescribed assumptions of measurement error and a priori uncertainty, the Degrees of Freedom for Signal (DFS) is adopted as a quantitative metric to systematically analyse the response of ALH information content to variations in AOD, wavelength, surface reflectance, and observation geometry. On this basis, the enhancement in ALH retrieval capability provided by multi-angle observations and polarization information is further evaluated, offering theoretical support for subsequent retrieval algorithm development and observation strategy optimization.

3.1 Information Content Analysis

In the framework of optimal estimation theory (Hou et al., 2018), the relationship between the state vector x (containing n parameters) and the observation vector y (with m measurements) can be expressed as:

$$y = F(x) + \epsilon \quad (1)$$

where F is the forward model that describes the physical relationship between satellite observations and atmospheric parameters (such as ALH), x is the state vector to be retrieved, and ϵ represents the errors arising from forward model simulations and satellite measurements.

The retrieval uncertainty (posterior covariance matrix S) is related to the Jacobian matrix K, which characterizes the sensitivity of the observations to the state vector:

$$S^{-1} = K^T S_\varepsilon^{-1} K + S_a^{-1} \quad (2)$$

https://doi.org/10.5194/egusphere-2026-3503
Preprint. Discussion started: 25 June 2026

Here, S_ε denotes the measurement error covariance matrix, and S_a represents the a priori error covariance matrix. In practical retrievals, the construction of S_ε is of critical importance. It includes not only instrument measurement noise, but also uncertainties associated with the forward model. In this study, S_ε is defined as a diagonal matrix:

$$S_\varepsilon = diag\left(\sigma^2_{I,v_1}, \dots, \sigma^2_{I,v_M}, \sigma^2_{DoLP,v_1}, \dots, \sigma^2_{DoLP,v_M}\right) \quad (3)$$

where the radiance uncertainty is typically assumed to be 5% of the measured value (accounting for calibration errors), while the absolute uncertainty of the Degree of Linear Polarization (DoLP) is usually set to 0.005 for high-precision polarimeters such as HARP2 (Sienkiewicz et al., 2025). This weighting scheme ensures that polarization signals have a higher constraint weight under conditions of high aerosol loading.

The superscripts $v_1 - v_M$ are used to represent individual viewing angles in multi-angle observations. Accordingly, the measurement vector y can be expressed as:

$$y = \left[I_\lambda^{v_1}, \dots, I_\lambda^{v_M}, DOLP_\lambda^{v_1}, \dots, DOLP_\lambda^{v_M}\right]^T \quad (4)$$

To establish the relationship between the retrieved state and the true state, the averaging kernel matrix A is introduced:

$$A = \frac{\partial \hat{x}}{\partial x} = (K^T S_\epsilon^{-1} K + S_a^{-1})^{-1} K^T S_\epsilon^{-1} K \quad (5)$$

The trace of the averaging kernel matrix A (i.e., the sum of its diagonal elements) is defined as the Degrees of Freedom for Signal (DFS), which quantifies how much information about the retrieved parameters can be obtained from the satellite measurements. For a single state variable, the DFS value ranges between 0 and 1. If the DFS of an aerosol parameter is close to 0, it indicates that the measurements contain little to no information for retrieving that parameter. Conversely, a DFS value approaching 1 indicates that the observations provide substantial information and make a strong contribution to the retrieval process.

Using the Unified Linearized Vector Radiative Transfer Model (UNL-VRTM), satellite observations and their weighting functions (Jacobian matrices) with respect to retrieval parameters are simulated under various viewing geometries. UNL-VRTM is based on the VLIDORT model (Spurr 2006) and computes the Stokes vector $[I, Q, U, V]^T$, where I represents radiance, and Q and U denote the linear polarization components (Wang et al., 2014; Xu and Wang, 2019). In this study, the observation vector consists of radiance III and the DoLP, which is defined as:

$$DOLP = \frac{\sqrt{Q^2 + U^2}}{I} \quad (6)$$

Furthermore, the Jacobian of DoLP with respect to the state vector can be expressed as:

$$\frac{\partial DoLP}{\partial x} = -\frac{DoLP}{I}\frac{\partial I}{\partial x_i} + \frac{Q\frac{\partial Q}{\partial x_i} + U\frac{\partial U}{\partial x_i}}{I\sqrt{Q^2 + U^2}} \quad (7)$$

https://doi.org/10.5194/egusphere-2026-3503
Preprint. Discussion started: 25 June 2026

3.2 Aerosol and Surface Models

In radiative transfer calculations, aerosol scattering and absorption processes involve AOD (related to the extinction coefficient), single scattering albedo (SSA), and the scattering phase matrix. For aerosol particles, these optical properties are computed using a linearized Mie scattering code. The common input parameters shared by the Mie scattering code and the radiative transfer model include those defining the bimodal log-normal volume size distribution (see Eq. 8), namely the median radius (r) and variance (σ) for both fine and coarse modes, as well as the real and imaginary parts of the complex refractive index. These parameters are specified based on the study of Lee et al. (2015), as detailed in Table 1.

$$\frac{\mathrm{d}V(r)}{\mathrm{d}\ln r} = \sum_{i=1}^{2} \frac{C_{v,i}}{\sqrt{2\pi}\sigma_i} e^{-\frac{1}{2}\left(\frac{\ln r - \ln r_{vi}}{\sigma_i}\right)^2} \tag{8}$$

Here, r_{vi} and σ represent the median radius and standard deviation of the bimodal log-normal volume size distribution, respectively.

Aerosol Type	Complex Refractive Index	$r_{v1}; r_{v2}$ (μm)	$\sigma_1; \sigma_2$ (μm)	FMF	Reference
Smoke	1.52−0.021i	0.15; 3.25	0.40; 0.75	0.85	(Chen et al., 2021b; Lee et al., 2015)
Dust	1.53−0.008i	0.15; 1.90	0.40; 0.63	0.15	(Zeng et al., 2008)

Table 1 Microphysical properties of aerosols in forward modelling

The aerosol vertical distribution is assumed to follow a Gaussian-like profile (Spurr and Christi, 2014), defined as:

$$\tau(z) = K \frac{\exp\left(-\sigma|z - z_{peak}|\right)}{[1 + \exp\left(-\sigma|z - z_{peak}|\right)]^2} \tag{9}$$

where K is related to the column aerosol loading; z_{peak} represents the height of the AOD peak, i.e., the ALH; and σ_t denotes the aerosol layer thickness, which is set to 1.76 km.

The surface reflectance is modelled using the kernel-driven BRDF model coupled within UNL-VRTM(Litvinov et al., 2011; Wang et al., 2014), expressed as:

$$\rho_{\mathrm{R}}(\mu, \mu_0, \Delta\phi, \lambda) = f_{iso}(\lambda) + f_{\mathrm{vol}}(\lambda) K_{\mathrm{vol}}(\mu, \mu_0, \Delta\phi) + f_{\mathrm{geo}}(\lambda) K_{\mathrm{geo}}(\mu, \mu_0, \Delta\phi) \tag{10}$$

Where μ, μ_0 and $\Delta\phi$ denote the solar zenith angle, viewing zenith angle, and relative azimuth angle, respectively; $K_{\mathrm{vol}}(\mu, \mu_0, \Delta\phi)$ is the volumetric scattering kernel derived from the Ross-Thick radiative transfer model; $K_{\mathrm{geo}}(\mu, \mu_0, \Delta\phi)$ is the geometric kernel derived from the Li-Sparse geometric-optical model (Wanner et al., 1995). The coefficients f_{iso}, f_{vol} and f_{geo} are BRDF kernel weights, obtained as the average values of the corresponding parameters for pixels with AOD > 0.3 from the MCD43A1 product over the study region. For surface polarized reflectance, the Bidirectional Polarization

https://doi.org/10.5194/egusphere-2026-3503
Preprint. Discussion started: 25 June 2026

Distribution Function (BPDF) kernel for land surfaces developed by Maignan et al.(2009), based on long-term PARASOL observations, is adopted. The kernel function is given as follows:

$$f_{\text{maignan}}(\theta, \theta_0, \Delta\phi) = \frac{C e^{-(\nu+\tan\gamma)}}{4(\mu_0+\mu)} \boldsymbol{F}_{\text{r}}(\gamma, m) \quad (11)$$

Where C is a constant characterizing the surface type; ν denotes the normalized difference vegetation index (NDVI), and the values of C and ν are given in Table 2; m is the refractive index of the vegetation canopy, typically set to 1.5. $\boldsymbol{F}_{\text{r}}(\gamma, m)$ represents the Fresnel reflection matrix with eight non-zero elements (Kokhanovsky et al., 2015).

Surface Type	C	ν	Reference
Vegetation	6.57	0.62	(Chen et al., 2021b)
Bare soil	7.29	0.03	(Chen et al., 2021b; Maignan et al., 2009)

Table 2 Surface model parameters

3.3 Sensitivity Analysis and Evaluation of ALH Retrieval

To systematically evaluate the retrievability of ALH under different observational conditions, this section employs an information content analysis approach to investigate how ALH information varies with AOD, observation wavelength, and surface reflectance under smoke aerosol conditions.

Fig. 1 presents the two-dimensional distributions of ALH–AOD–DFS for four spectral bands (441 nm, 549 nm, 669 nm, and 873 nm) at a scattering angle of $\theta = 120^{\circ}$, under different surface reflectance conditions $A_s = 0.00,\ 0.05,\ 0.20,\ 0.50$. From the spectral perspective (comparison by columns), the information content of ALH shows a clear decreasing trend with increasing wavelength, i.e., 441 nm > 549 nm > 669 nm > 873 nm. Under typical aerosol loading conditions (AOD = 0.3–1), the DFS at 441 nm generally reaches 0.6–1.0, whereas at 873 nm it is typically only 0.2–0.5, corresponding to an overall reduction of approximately 40%–70% in information content. In comparison, the 549 nm and 669 nm bands fall within an intermediate range, with DFS values around 0.4–0.7. These results indicate that shorter wavelengths have a clear advantage for ALH retrieval. This behaviour is primarily attributed to stronger Rayleigh scattering at shorter wavelengths, which enhances the sensitivity of the radiative field to changes in atmospheric vertical structure. In contrast, molecular scattering weakens at longer wavelengths, leading to a significant reduction in sensitivity to layer height. This finding is highly consistent with previous studies (Wu et al., 2016), which identified near-ultraviolet and blue bands as the optimal spectral regions for ALH retrieval using multi-angle polarization measurements.

https://doi.org/10.5194/egusphere-2026-3503
Preprint. Discussion started: 25 June 2026

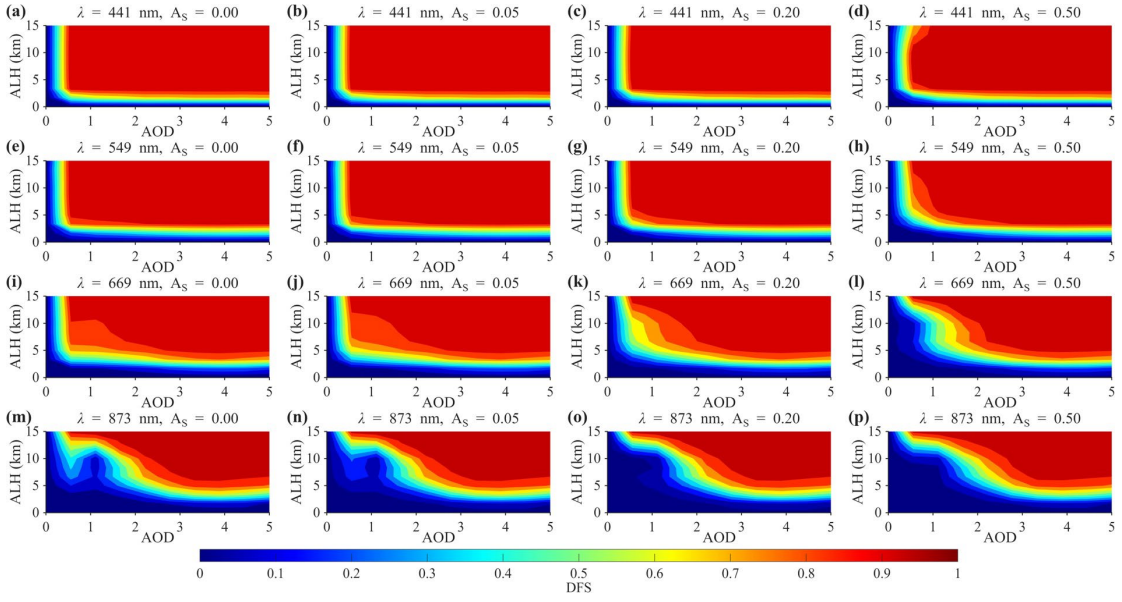

Fig. 1. Characteristics of ALH-AOD-DFS distributions derived from radiance under different spectral bands and surface reflectance conditions. Rows correspond to wavelengths of 441 nm, 549 nm, 669 nm, and 873 nm, respectively, while columns represent different surface reflectance conditions ($A_s = 0.00, 0.05, 0.20, 0.50$). Colors indicate the DFS values of ALH, ranging from 0 to 1.

From the perspective of surface reflectance, it exerts a significant suppressing effect on ALH information content, with clear spectral dependence. The shortwave bands (441 nm and 549 nm) exhibit remarkable stability: even as surface reflectance A_s increases from 0 to 0.50, the DFS distributions for these bands remain almost entirely saturated (DFS > 0.9). This indicates that, at short wavelengths, atmospheric scattering dominates over surface reflection, and the extraction of ALH information is minimally affected by surface background. High sensitivity can thus be maintained even under low AOD conditions. In contrast, the longer wavelengths (669 nm and 873 nm) show pronounced degradation. As A_s increases, the DFS values for these bands decrease significantly, and the effective sensitivity region under low to moderate aerosol loading (AOD < 1.0) rapidly shrinks. Under dark surface conditions ($A_s \leq 0.05$), regions with DFS > 0.5 can cover most of the range where AOD≈0.5. However, under high-reflectance surfaces ($A_s \geq 0.2$), a significant information response appears only when AOD > 1.0. This behaviour arises from the competition between atmospheric scattering and surface reflection. At short wavelengths such as 441 nm, both Rayleigh scattering and aerosol scattering cross-sections are large, meaning that most of the radiance received by the sensor originates from atmospheric scattering rather than surface reflection. As a result, variations in layer height strongly modulate the signal, and the surface background is effectively "screened out." As wavelength increases, atmospheric scattering weakens; when surface reflectance becomes stronger, its contribution to the total radiance increases, causing the ALH signal to be increasingly masked by the bright background. Therefore, shortwave bands are critical for achieving reliable ALH retrievals over high-reflectance land surfaces, whereas longer wavelengths exhibit a much stronger dependence on aerosol loading.

https://doi.org/10.5194/egusphere-2026-3503
Preprint. Discussion started: 25 June 2026

From the AOD perspective, the DFS exhibits a clear stage-wise behavior along the AOD dimension. When AOD is low (< 0.3), the DFS is close to zero, indicating that layer height information is difficult to detect. As AOD increases to the range of 0.5–1.5, the DFS rises rapidly, and under high aerosol loading conditions (> 2), the DFS tends to saturate. This pattern suggests the existence of a distinct aerosol loading threshold for ALH retrieval. When aerosol concentrations are insufficient, atmospheric scattering signals are weak and surface reflection dominates the total radiance. As a result, variations in layer height have only a limited impact on top-of-atmosphere radiation, making it difficult to extract ALH information from the observations.

Along the ALH dimension, the DFS generally shows a slight increase with increasing layer height, indicating that elevated aerosol layers are easier to detect than near-surface aerosols. This is because higher-altitude aerosols exert a stronger modulation on the solar radiation path and exhibit stronger coupling with molecular scattering layers, making the radiance more sensitive to height variations. In contrast, low-level aerosols are more easily masked by surface reflection contributions, leading to weaker sensitivity to layer height.

Overall, the information content for ALH retrieval exhibits significant variability across different observation conditions. Under scenarios characterized by high aerosol loading (AOD > 1), short wavelengths ($\leq 550\,nm$), and dark surfaces ($A_s \leq 0.05$), the DFS consistently exceeds 0.6, indicating robust retrieval capability. Conversely, under conditions of low aerosol loading (AOD < 0.3), long wavelengths ($> 550\,nm$), and bright surfaces ($A_s \geq 0.20$), the DFS typically falls below 0.3, leading to a substantial increase in retrieval uncertainty.

3.4 Enhancement of ALH Information Content by Polarization under Multi-Viewing Geometries

Under fixed conditions of solar zenith angle ($SZA = 40°$) and aerosol optical depth ($AOD = 0.3$), Figs. 2-6 present the ALH–DFS distributions for different viewing zenith angles ($VZA = 0°$、$20°$、$40°$、$60°$、$80°$) and surface reflectance conditions. These figures are used to compare two observation configurations: radiance-only (*I*) and combined radiance and polarization (*I*+*P*). In each figure, the upper panels show DFS derived using only radiance, while the lower panels show DFS derived using both radiance and polarization (*I*+*P*). The columns correspond to different surface reflectance values ($A_s = 0.00,\ 0.05,\ 0.20,\ 0.500$). Overall, under moderate aerosol loading conditions (AOD = 0.3), the ALH information content is relatively low when using radiance-only observations, and it is strongly affected by surface reflectance. Over dark surfaces ($A_s \leq 0.05$), the DFS still maintains a certain level; however, as surface reflectance increases, the DFS decreases significantly. In particular, under high-reflectance conditions ($A_s = 0.50$), the sensitivity of radiance to layer height is greatly reduced. This indicates that under moderate aerosol loading, surface reflection exerts a strong masking effect on the scalar radiation field, thereby weakening the detectability of ALH.

https://doi.org/10.5194/egusphere-2026-3503
Preprint. Discussion started: 25 June 2026

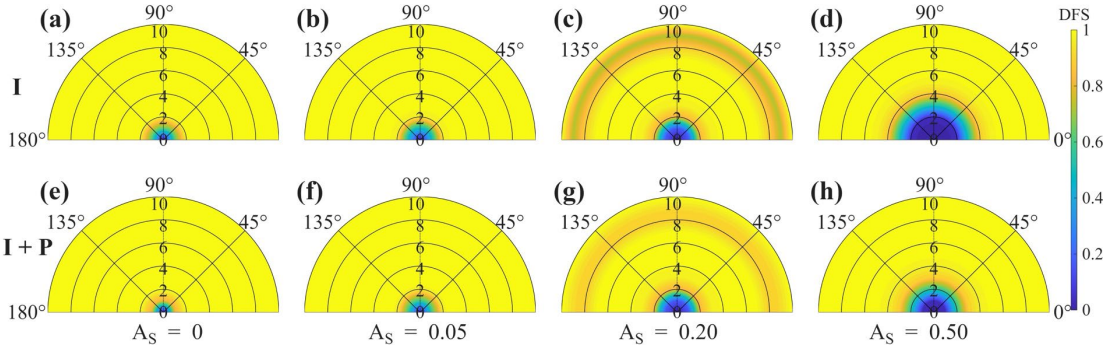

Fig. 2. Comparison of ALH-DFS distributions under different combinations of observational information (I vs. I+P) and surface reflectance conditions, with VZA = 0°, SZA = 40°, and AOD = 0.3. The top row shows DFS calculated using radiance (I) only, while the bottom row shows DFS obtained by combining radiance and polarization information (I+P). Columns correspond to different surface reflectance values ($A_s = 0.00,\ 0.05,\ 0.20,\ 0.50$).

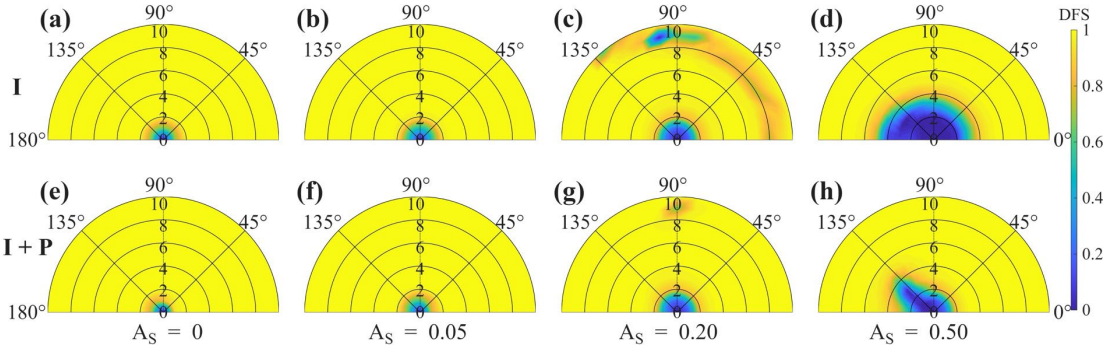

Fig. 3. Same as Fig. 2, but with VZA = 20°.

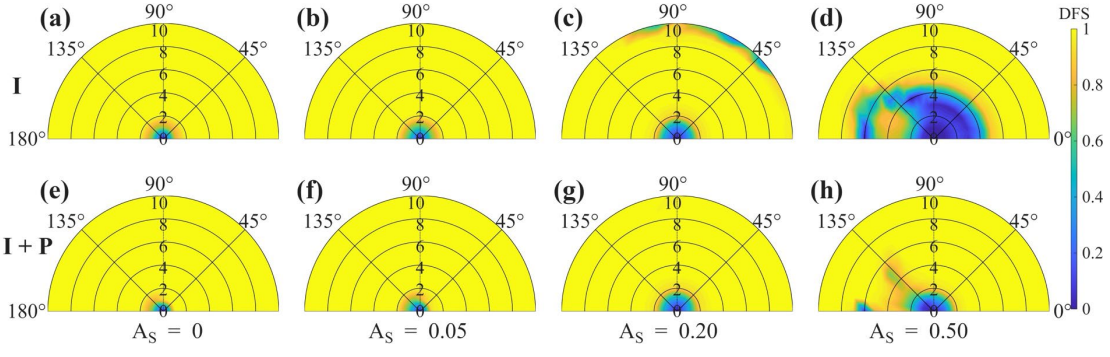

Fig. 4. Same as Fig. 2, but with VZA = 40°.

https://doi.org/10.5194/egusphere-2026-3503
Preprint. Discussion started: 25 June 2026

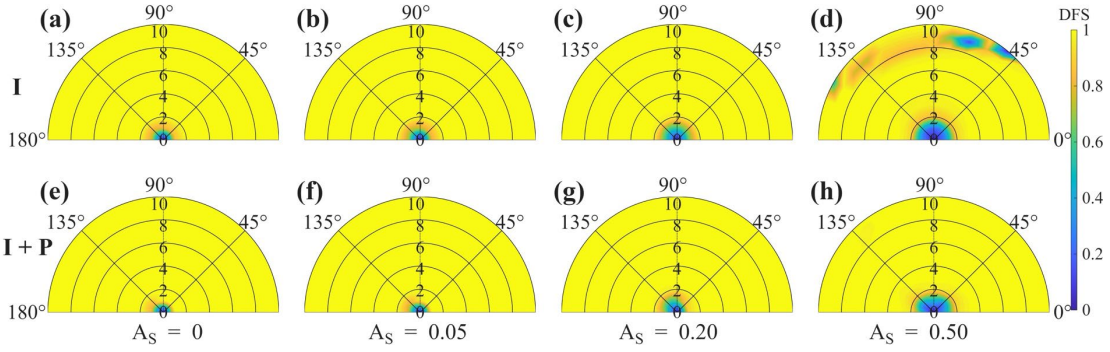

Fig. 5. Same as Fig. 2, but with VZA = 60°

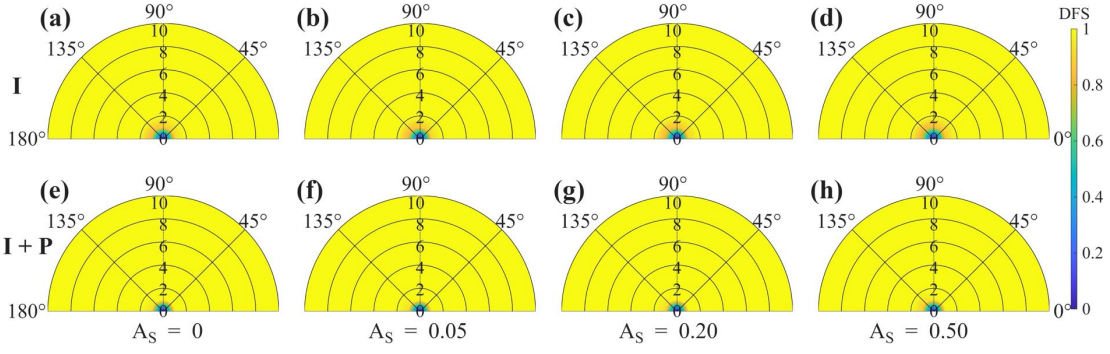

Fig. 6. Same as Fig. 2, but with VZA = 80°.

After incorporating polarization information (*I*+*P*), the information content of ALH is improved across all viewing geometries, with particularly pronounced enhancements over high-reflectance surfaces. For example, at $VZA = 40^{\circ}$ and $A_s = 0.50$ (comparing Figs. 4(d) and (h)), the inclusion of polarization increases the DFS from approximately 0.2 to the range of 0.5–0.7, corresponding to an information gain of about 0.5. This improvement arises from the strong sensitivity of polarization signals to atmospheric scattering components, which effectively suppresses the interference from surface reflection. As a result, even under complex background conditions with $A_s = 0.20 - 0.50$, the ALH DFS can still be maintained above the retrievability threshold of 0.5, demonstrating the substantial advantage of incorporating polarization information in ALH retrieval.

In addition, DFS exhibits a pronounced enhancement with viewing geometry, and this effect becomes more evident when polarization information is included. As *VZA* increases from 0° to 80°, the atmospheric path length is effectively extended, leading to a stronger contribution from atmospheric scattering. Under the *I*+*P* configuration, the high-DFS region (DFS > 0.8, shown in yellow) associated with large viewing angles (VZA > 40°) expands significantly. Even under extremely high surface reflectance conditions ($A_s = 0.50$), large-angle polarimetric observations are still able to maintain DFS values above

https://doi.org/10.5194/egusphere-2026-3503
Preprint. Discussion started: 25 June 2026

0.6. This indicates that ALH information content is jointly controlled by observation geometry and surface reflectance, while polarization information effectively mitigates the adverse influence of surface background on layer height retrieval.

Overall, the comparison demonstrates that the inclusion of polarization observations introduces an additional independent physical dimension, which not only significantly enhances the overall sensitivity to ALH, but also substantially reduces the dependence of the retrieval on specific viewing geometries and low surface reflectance conditions. As a result, the retrieval algorithm is able to robustly extract ALH information over a much wider range of surface types and observation angles.

3.5 Impact of Viewing Geometry and Polarization Information on DFS

This subsection compares the effects of the number of viewing angles and observation modes (*I* and *I*+*P*) on the DFS under different surface reflectance conditions ($A_s = 0.00,\ 0.05,\ 0.20,\ 0.50$).

As shown in Fig. 7, polarization observations provide a significant enhancement in system information content. In all simulated scenarios, the DFS values corresponding to the radiance-plus-polarization configuration (red curves, *I*+*P*) are consistently higher than those derived from radiance-only observations (blue curves, *I*). Quantitatively, for typical configurations with 3 – 6 viewing angles, the inclusion of polarization information leads to an increase in DFS of approximately 5% – 30%. This enhancement becomes more pronounced over high-reflectance surfaces ($A_s = 0.50$), indicating a higher information contribution efficiency of polarization measurements under bright surface conditions. These results demonstrate that polarization observations can effectively enhance the sensitivity of atmospheric parameters and, to a certain extent, suppress the interference caused by surface reflection.

In addition, DFS exhibits a clear saturation tendency with increasing number of viewing angles. As the number of angles increases from 1 to approximately 5, the DFS under all scenarios undergoes a rapid growth phase, during which more than 70% of the total information gain is typically achieved. However, when the number of viewing angles exceeds 6, the slope of the curve decreases markedly and the growth of information content becomes gradual. This result is consistent with the findings of Chen et al. (2021b), highlighting the nonlinear nature of information acquisition in multi-angle observations. These results suggests that multi-angle measurements provide the most significant information gain at the early stage, whereas beyond a certain number of viewing geometries, the system approaches information saturation and the marginal benefit of additional angles gradually diminishes (Gu et al., 2022).

Finally, the complexity of the surface environment imposes a direct constraint on the information content of the signal. As A_s increases from 0 to 0.5, the overall DFS decreases by approximately 10%–40%, while the shadowed region associated with *SZA* variations expands significantly. This indicates that under high-reflectance surfaces (e.g., desert regions), atmospheric signals are more easily overwhelmed by surface contributions, making the retrieval more sensitive to observation geometry. Therefore, in such complex surface environments, the incorporation of combined multi-angle and polarization observations can substantially improve the stability and robustness of retrieval results.

https://doi.org/10.5194/egusphere-2026-3503
Preprint. Discussion started: 25 June 2026

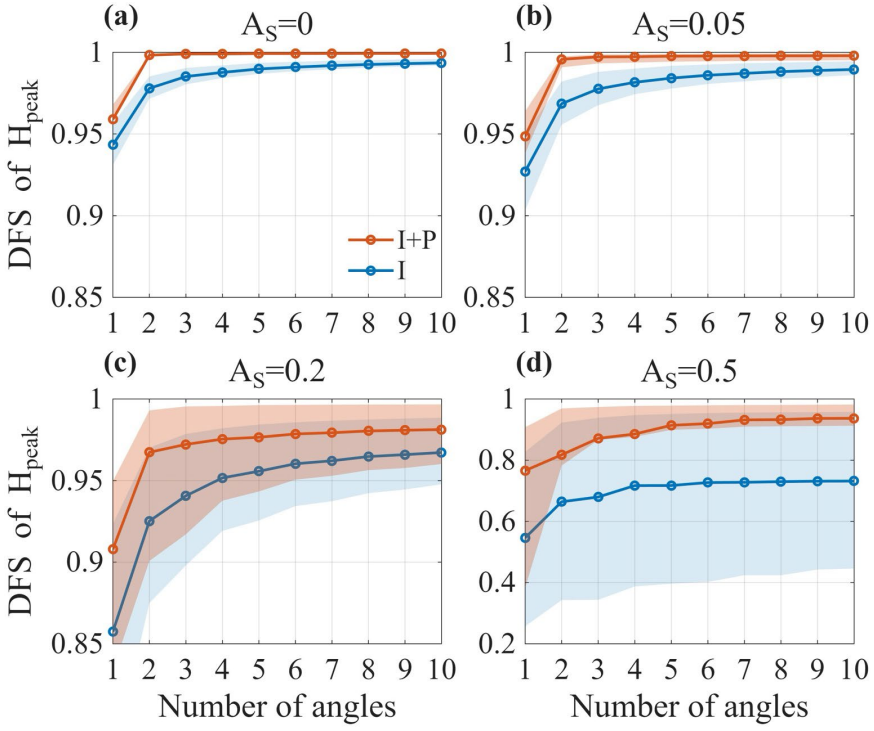

Fig. 7. Influence of the number of viewing angles and polarization information on the DFS under different surface reflectance conditions A_s. Panels (a)-(d) correspond to surface reflectance values of 0, 0.05, 0.20, and 0.50, respectively. Red curves represent joint observations of radiance and polarization (I+P), while blue curves correspond to radiance-only (I) observations. Shaded areas indicate the variation of DFS due to SZA changes within the range of 25° to 60°.

4 Synergistic ALH Retrieval Method Combining Multi-angle and Polarimetric Observations

Multi-angle polarimetric remote sensing observations provide important constraints for aerosol vertical structure retrieval. Unlike traditional passive remote sensing methods that rely solely on radiance information, polarization signals are primarily generated by atmospheric scattering processes and exhibit higher sensitivity to aerosol microphysical properties as well as their vertical distribution. In particular, at short wavelengths, Rayleigh scattering by atmospheric molecules makes a significant contribution, enhancing the sensitivity of TOA polarization signals to changes in ALH.

When the ALH varies, the optical thickness of the overlying molecular layer changes accordingly, which in turn modifies the coupling between Rayleigh scattering and aerosol scattering, leading to variations in TOA polarized radiance. A higher aerosol layer can partially attenuate or shield the polarization signal generated by Rayleigh scattering, making the observed polarization state more sensitive to ALH (Wu et al., 2016). Therefore, polarization observations provide effective information constraints for ALH retrieval.

Under multi-angle observation conditions, different viewing geometries correspond to different scattering angles, thereby sampling different portions of the aerosol scattering phase function and polarization phase function. By jointly exploiting

https://doi.org/10.5194/egusphere-2026-3503
Preprint. Discussion started: 25 June 2026

multi-angle radiance and polarization information, the ability to retrieve aerosol optical properties and their vertical distribution can be significantly improved. Based on this physical mechanism, this study utilizes multi-angle polarimetric observations at 441 nm to simulate aerosol–molecular coupled scattering processes using a radiative transfer model, and retrieves ALH through an optimal estimation approach.

For forward modelling, this study uses the UNL-VRTM radiative transfer model to compute TOA Stokes parameters under different ALH conditions, including radiance I and polarization components Q and U. Circular polarization (Stokes parameter V) is generally negligible in atmospheric studies (Gassó and Knobelspiesse, 2022).

To improve computational efficiency, a forward-model LUT is first constructed using the radiative transfer model, and simulated results corresponding to specific observation geometries are obtained through multidimensional interpolation. The LUT node settings are provided in Table 3. Subsequently, a cost function is defined to quantify the discrepancy between simulated and observed values:

$$\chi^2 = \frac{1}{N}\sum_{i}^{N}\left[\frac{(I_{meas}-I_{calc})^2}{\sigma_I^2(i)} + \frac{(Q_{meas}-Q_{calc})^2}{\sigma_Q^2(i)} + \frac{(U_{meas}-U_{calc})^2}{\sigma_U^2(i)}\right] \quad (12)$$

where the selected wavelength is 441 nm, N denotes the total number of multi-angle observations (here $N = 10$); the subscripts *meas* and *calc* represent satellite observations and model simulations, respectively; σ denotes the standard deviation. By computing the cost function under different ALH conditions and identifying the solution that minimizes χ^2, the optimally estimated ALH can be retrieved.

Variable	Number of nodes	Node
SZA	8	$0^\circ, 10^\circ, \ldots, 70^\circ$
VZA	8	$0^\circ, 10^\circ, \ldots, 70^\circ$
RAA	19	$0^\circ, 10^\circ, \ldots, 180^\circ$
AOD (550 nm)	8	0.1, 0.3, 0.5, 1.0, 2.0, 3.0, 4.0, 5.0
ALH	8	0, 1, 2, 3, 5, 7, 10, 15 km
Surface Albedo	5	0, 0.05, 0.1, 0.2, 0.3

Table 3 LUT nodes for the forward model

5 ALH Retrieval Results and Accuracy Evaluation

To systematically evaluate the reliability of ALH products retrieved from HARP2 multi-angle polarimetric observations, this study selects six representative aerosol transport cases, including three biomass burning smoke events over North America and three dust transport events over West Africa. Smoke aerosols from biomass burning are typically strongly absorbing, and their vertical distribution is influenced by fire intensity, atmospheric convection, and long-range transport processes. In contrast, mineral dust aerosols are primarily generated from surface dust emission in arid and semi-arid regions, and can

https://doi.org/10.5194/egusphere-2026-3503
Preprint. Discussion started: 25 June 2026

form large-scale transboundary plumes under the influence of synoptic circulation and the Saharan Air Layer (SAL). These two aerosol types exhibit pronounced differences in optical properties, particle size distribution, and vertical structure, providing ideal cases for evaluating the applicability of the retrieval algorithm under different aerosol conditions.

First, aerosol transport processes are identified using VIIRS true-colour imagery. The ALH results retrieved from HARP2 are then compared with the TROPOMI Level-2 ALH product, and further validated against lidar observations from the ATLID instrument onboard the EarthCARE satellite. By combining case-based analysis with statistical evaluation metrics, the spatial distribution characteristics and error behaviour of different retrieval products are systematically examined, thereby assessing the performance of HARP2 multi-angle polarimetric observations in ALH retrieval.

All ALH values used in this study—including the TROPOMI ALH product, ATLID-derived ALH calculated using extinction-weighted profiles, and HARP2-retrieved ALH—are defined relative to mean sea level.

5.1 Biomass Burning Smoke Events

In recent years, frequent large-scale wildfires in North America have become a major factor affecting regional air quality and climate. Large amounts of smoke aerosols generated by fires can be uplifted into the middle and upper troposphere under strong convection and thermal buoyancy, and subsequently transported across regions or even intercontinentally by the westerly circulation (Peterson et al., 2018). The vertical distribution of smoke aerosols directly affects their radiative forcing and aerosol–cloud interactions; therefore, accurate retrieval of smoke layer height is essential for understanding their climatic impacts.

This study selects three representative smoke transport events over North America on May 28, May 30, and June 1, 2025. These cases are designed to capture different physical stages and vertical evolution characteristics of smoke transport. The selected days cover a range of scenarios, including multilayer smoke plumes transported in the upper troposphere in late May, rapid expansion of smoke coverage at the end of May, and lower-tropospheric advection processes in early June. Such diverse smoke distributions, spanning from upper to lower troposphere and from local to regional scales, provide an ideal dataset for systematically evaluating the stability, spatial continuity, and altitude-dependent performance of the retrieval algorithm under complex atmospheric conditions.

5.1.1 The North American Smoke Event of May 28, 2025

In late May 2025, multiple wildfires occurred in western and central Canada. Under the influence of prevailing westerly winds and large-scale atmospheric circulation, a substantial amount of smoke aerosols was transported to the central and eastern regions of North America, forming a pronounced long-range transport plume (Fromm et al., 2010). The smoke exhibited a multilayer vertical structure within the troposphere, accompanied by the development of localized deep convective cloud systems. Such complex atmospheric conditions impose more stringent requirements on passive remote sensing retrievals of ALH. Therefore, this case provides an effective test for evaluating the robustness and stability of different retrieval methods under highly complex atmospheric environments.

https://doi.org/10.5194/egusphere-2026-3503
Preprint. Discussion started: 25 June 2026

As shown in Fig. 8(a), a large-scale smoke transport event occurred over North America on May 28, 2025. The VIIRS true-colour imagery clearly reveals a band-shaped smoke plume extending eastward from western Canada and traversing central Canada. The smoke exhibits a spatially continuous pattern characteristic of long-range transport. Figs. 8(b–c) show that the ALH retrieved from HARP2 and the ALH product from TROPOMI exhibit similar spatial distribution patterns, indicating a general consistency between the two retrieval results in capturing the smoke layer structure.

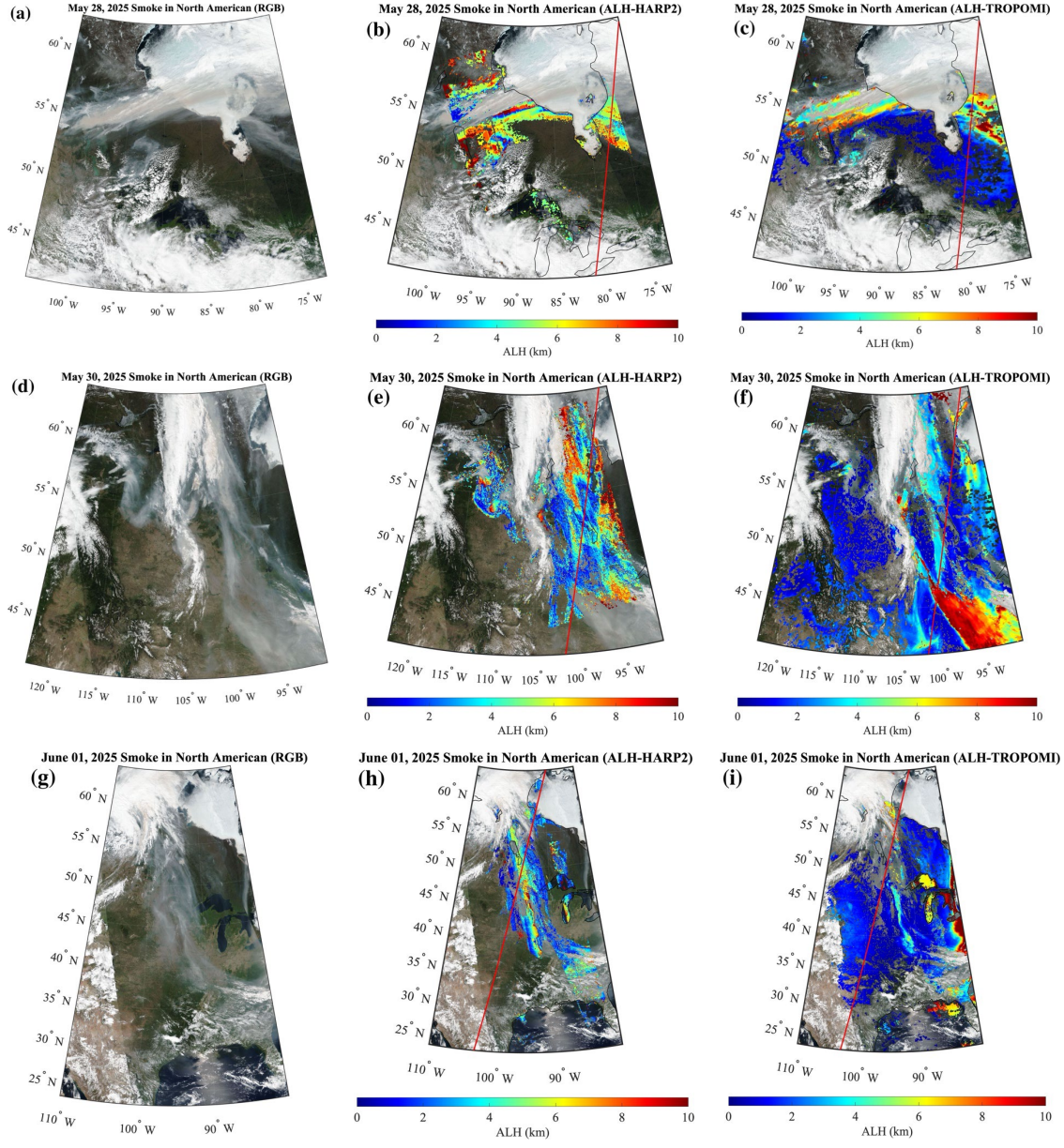

Fig. 8. Examples of retrieval for smoke cases. The first column presents the corresponding true-colour images from VIIRS/Suomi-NPP. The second column displays the UVD-derived ALH relative to sea level with the red line representing the EarthCARE track. The third column presents the TROPOMI Level 2 ALH product.

https://doi.org/10.5194/egusphere-2026-3503
Preprint. Discussion started: 25 June 2026

To quantitatively evaluate the retrieval results, Fig. 9(a) presents the ALH comparison along the EarthCARE orbit. ATLID lidar observations indicate a multilayer aerosol structure in this region, with smoke aerosol centroid heights primarily distributed in the 4–6 km range, and locally showing vertically developing aerosol layers. The comparison shows that ALH retrieved from HARP2 (cyan) is generally consistent with ATLID observations and successfully captures the vertical variability of the smoke layer. In the latitude range of $52°N - 56°N$, the HARP2-derived heights are in good agreement with the smoke layer center height observed by ATLID. In contrast, ALH retrieved from TROPOMI (magenta) is systematically lower, reaching values of only 1–2 km in some regions, which is significantly below the smoke layer heights observed by ATLID.

This discrepancy may be attributed to the fact that the TROPOMI retrieval relies on O_2A band absorption features, whose sensitivity to ALH is easily affected by highly reflective underlying surfaces. Under bright surface conditions, strong surface-reflected radiation reduces the effective atmospheric absorption path length, causing the algorithm to interpret the mixed signal as originating from a lower atmospheric layer, thereby leading to an underestimation of layer height (Nanda et al., 2020). In contrast, HARP2 multi-angle polarimetric observations can effectively suppress surface reflection signals by exploiting the inherent sensitivity of polarization to atmospheric scattering. Owing to its strong sensitivity to aerosol polarization signatures, HARP2 demonstrates greater robustness in identifying elevated smoke layers under complex surface and atmospheric conditions.

5.1.2 The North American Smoke Event of May 30, 2025

During the observations on May 30, 2025, a pronounced smoke transport event was again observed over North America, with the spatial extent of the smoke further expanding and posing potential impacts on regional radiative balance and air quality. As shown in Fig. 8(d), the smoke is primarily distributed over central Canada (approximately $100°W - 105°W$), forming a continuous zonal plume structure along the north–south direction at higher altitudes.

In the typical smoke region near the EarthCARE ground track, ALH-HARP2 and ALH-TROPOMI exhibit strong spatial consistency (Figs. 8(e–f)), both successfully capturing the prominent banded smoke plume. In terms of horizontal details, the TROPOMI retrieval shows finer spatial texture, clearly resolving internal variability within the smoke plume. In regions with high AOD, strong spectral absorption features provide TROPOMI with robust constraints on layer height.

Further examination of the vertical cross-section in Fig. 9(b) shows that within the latitude range of $46°N$ to $60°N$, the retrievals from both HARP2 and TROPOMI are in good vertical agreement with ATLID observations, all concentrated around 4 km. This indicates that for dense smoke layers, both the HARP2 multi-angle polarimetric method proposed in this study and the TROPOMI O_2A band method can retrieve ALH with high accuracy and robustness.

https://doi.org/10.5194/egusphere-2026-3503
Preprint. Discussion started: 25 June 2026

5.1.3 The North American Smoke Event of June 1, 2025

In early June 2025, continued wildfire activity over North America led to further transport of smoke aerosols toward the central and eastern United States. In this case, the overall smoke layer height was relatively low, primarily distributed in the lower and middle troposphere. Such a low-altitude transport scenario provides an important case for evaluating the applicability of retrieval algorithms across different altitude ranges.

As shown in Figs. 8(h–i), both ALH-HARP2 and ALH-TROPOMI identify a relatively high-value region between $90^{\circ}W$ and $100^{\circ}W$. The HARP2 retrieval indicates that the smoke layer is mainly distributed within the 2–4 km range, with some areas reaching up to approximately 5 km, reflecting transport in the lower-to-middle troposphere. In comparison, although the TROPOMI ALH product successfully captures the spatial extent of the smoke plume, its overall height estimates are noticeably lower.

Comparison with ATLID vertical profiles (Fig. 9(c)) shows that the main smoke layer is located between 2–4 km. The HARP2 retrieval is generally consistent with ATLID observations. However, the TROPOMI retrieval in the latitude range of $37°N - 44°N$ is biased toward near-surface values, exhibiting a significant systematic underestimation of ALH.

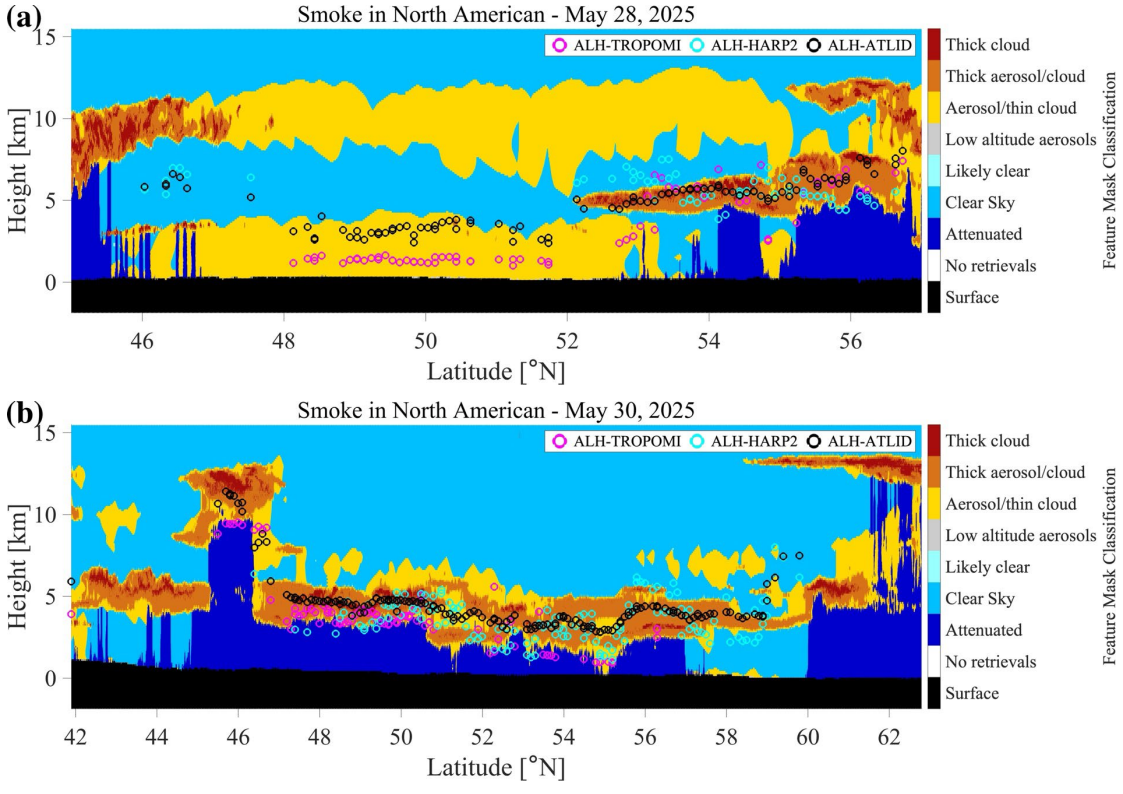

https://doi.org/10.5194/egusphere-2026-3503
Preprint. Discussion started: 25 June 2026

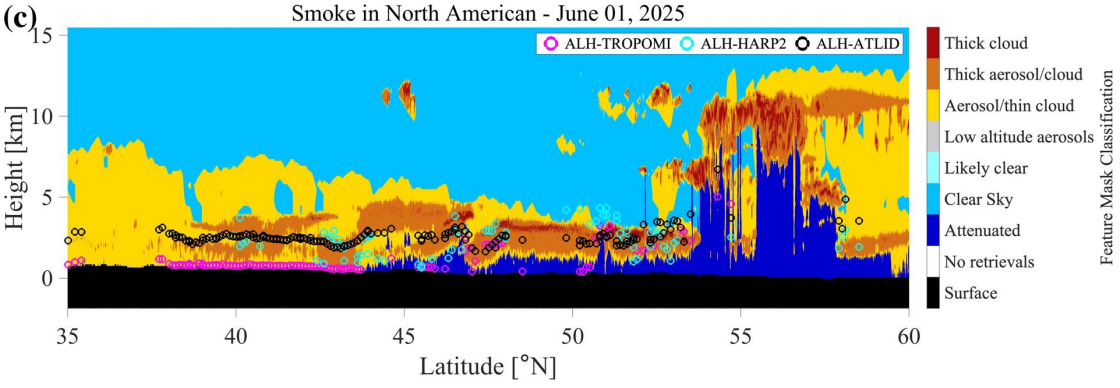

Fig. 9. Comparison of ALH-HARP2 and ALH-TROPOMI with the corresponding ATLID measurements for smoke cases on the feature classification curtain plot. Panels (a)-(c) present comparisons of ALH-HARP2 and ALH-TROPOMI with ATLID in three smoke cases, respectively.

5.2 Dust Transport Events

The Sahara Desert is one of the largest sources of mineral dust in the world, emitting vast amounts of aerosols to the Atlantic Ocean and West Africa each year. During spring and summer, under the influence of the SAL and atmospheric systems such as African easterly waves, dust can be uplifted to altitudes of several kilometers and transported over long distances (Doherty et al., 2008; Prospero et al., 2014). The height of the dust layer not only affects its radiative forcing but also plays an important role in cloud formation processes. To evaluate the applicability of the retrieval algorithm under mineral dust conditions, this study selects three representative dust transport events over West Africa on March 18, May 30, and September 17, 2025.

5.2.1 Near-Coastal Low-Level Dust Transport Event on March 18, 2025

This case occurred along the West African coastal region and represents a typical near-shore dust transport process. The dust is primarily controlled by near-surface mixing processes and transport by the northeast trade winds, forming a relatively shallow aerosol layer (approximately 2 – 4 km) in the land–sea transition zone. This feature is consistent with previous understanding of the initial stage of SAL transport, in which dust is mainly distributed in the lower to middle troposphere near the source region and gradually evolves during transport (Kokhanovsky et al., 2015).

As shown in Fig. 10(a), a distinct dust transport band is observed along the West African coast and adjacent offshore regions, with dust spreading westward from the Sahara toward the Atlantic Ocean. The HARP2 retrieval results (Fig. 10(b)) identify relatively sparse and discrete ALH pixels near the ATLID track, with limited spatial coverage and heights mainly concentrated in the 2–4 km range. In contrast, the TROPOMI product (Fig. 10(c)) provides retrievals over a broader spatial extent.

From the ATLID profile comparison (Fig. 11(a)), the number of spatially collocated HARP2 pixels is relatively small and scattered, with most values overestimating ALH-ATLID by about 0.5–1 km. TROPOMI captures the general dust layer

https://doi.org/10.5194/egusphere-2026-3503
Preprint. Discussion started: 25 June 2026

height in the range of 2–3 km and shows overall good performance; however, a notable underestimation is observed in the latitude range of $14^{\circ}N - 16^{\circ}N$.

5.2.2 West African Dust Transport Event on May 30, 2025

In May, as the Intertropical Convergence Zone (ITCZ) shifts northward, the dust transport pathway correspondingly migrates to higher latitudes. This transition is governed by large-scale atmospheric circulation. During this stage, dust is no longer confined to the lower troposphere but is often injected into higher-altitude warm and dry air masses, forming the typical SAL structure, with longer transport distances and a broader vertical extent (Xu et al., 2017).

As shown in Fig. 10(d), the true-colour imagery reveals a pronounced arc-shaped dust plume extending from West Africa north-westward over the Atlantic Ocean. Both ALH-HARP2 and ALH-TROPOMI show low values (blue regions) south of $15^{\circ}N$, while consistently capturing elevated layer heights north of $15^{\circ}N$. Due to its reliance on VIIRS AOD products in the retrieval process, HARP2 is constrained by the overlap of valid observations between the two datasets. Although it achieves high accuracy over both land and ocean, its spatial coverage is somewhat more limited compared to the TROPOMI product.

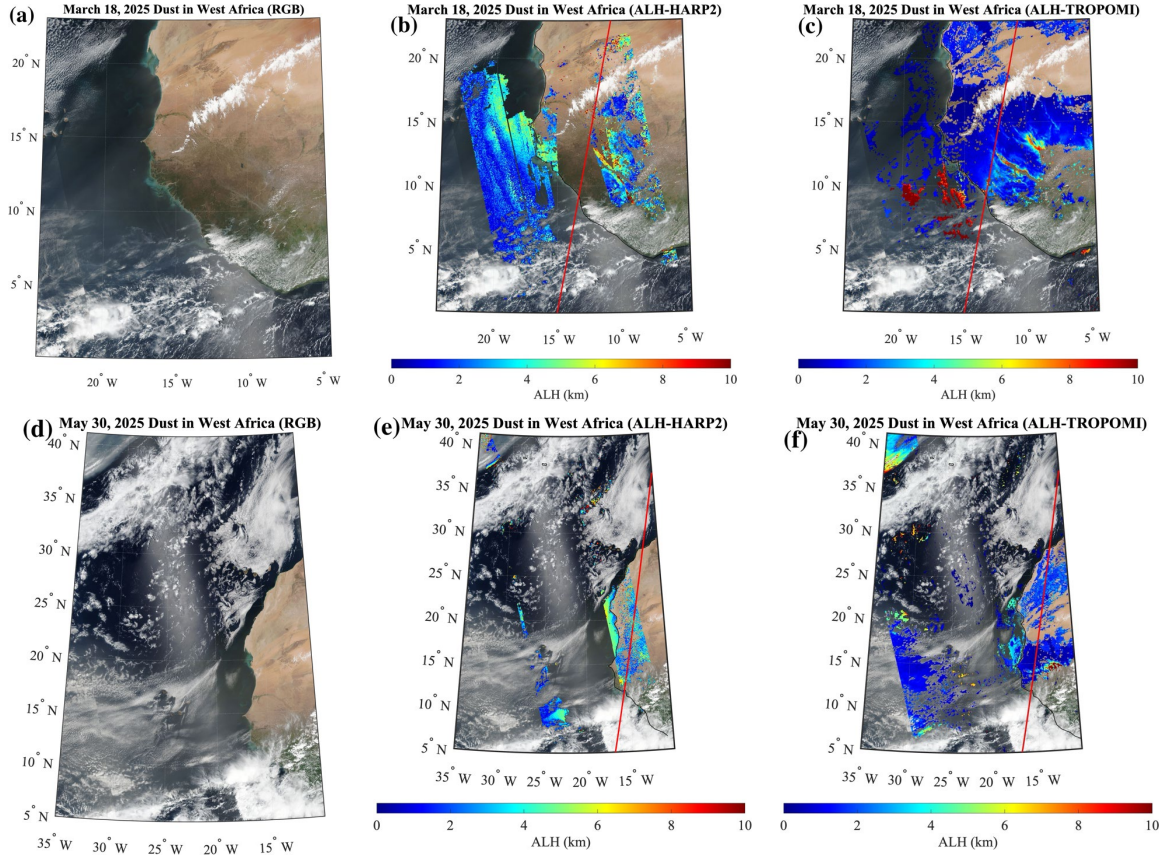

https://doi.org/10.5194/egusphere-2026-3503
Preprint. Discussion started: 25 June 2026

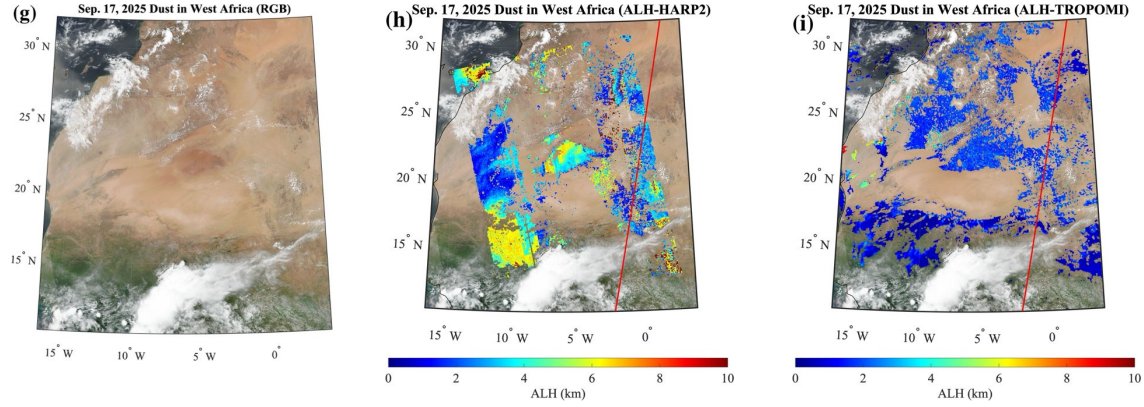

Fig. 10. Examples of retrieval for dust cases. The first column presents the corresponding true-colour images from VIIRS/Suomi-NPP. The second column displays the UVD-derived ALH relative to sea level with the red line representing the EarthCARE track. The third column presents the TROPOMI Level 2 ALH product.

Comparison with ATLID lidar observations indicates that the actual dust layer height is mainly distributed within the 3 – 5 km range. The HARP2 retrieval results fluctuate around the ATLID-derived ALH, demonstrating good overall agreement. This can be attributed to the strong sensitivity of the 441 nm polarization signal to non-spherical dust particles. Variations in polarization state enable more effective extraction of single-scattering contributions from the top of the aerosol layer (Dubovik et al., 2006), thereby significantly correcting the height underestimation commonly observed in traditional methods under SAL conditions and achieving consistency with ATLID active measurements. Notably, this bias characteristic has been observed in previous cases and is further confirmed in this event. In contrast, the TROPOMI product shows strong underestimation in the latitude range of $14^{\circ}N - 17^{\circ}N$, with retrieved values close to the surface (errors exceeding 2 km). In other regions, a moderate underestimation of about 0.5 km is also observed. This systematic low bias reflects the limitations of single absorption-band methods in handling optically thick aerosol layers (Sanders et al., 2015). When strong multiple scattering occurs within the dust layer, absorption-based techniques alone often struggle to distinguish between the layer top and the internal centroid height.

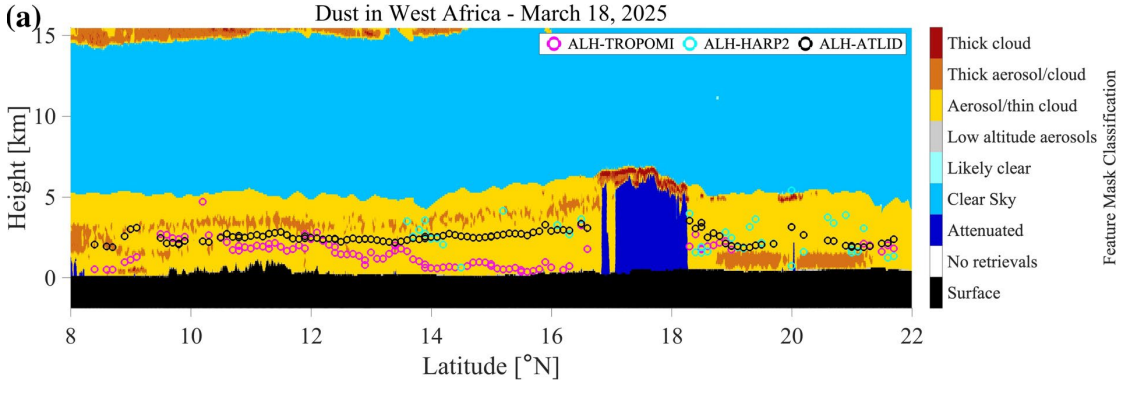

https://doi.org/10.5194/egusphere-2026-3503
Preprint. Discussion started: 25 June 2026

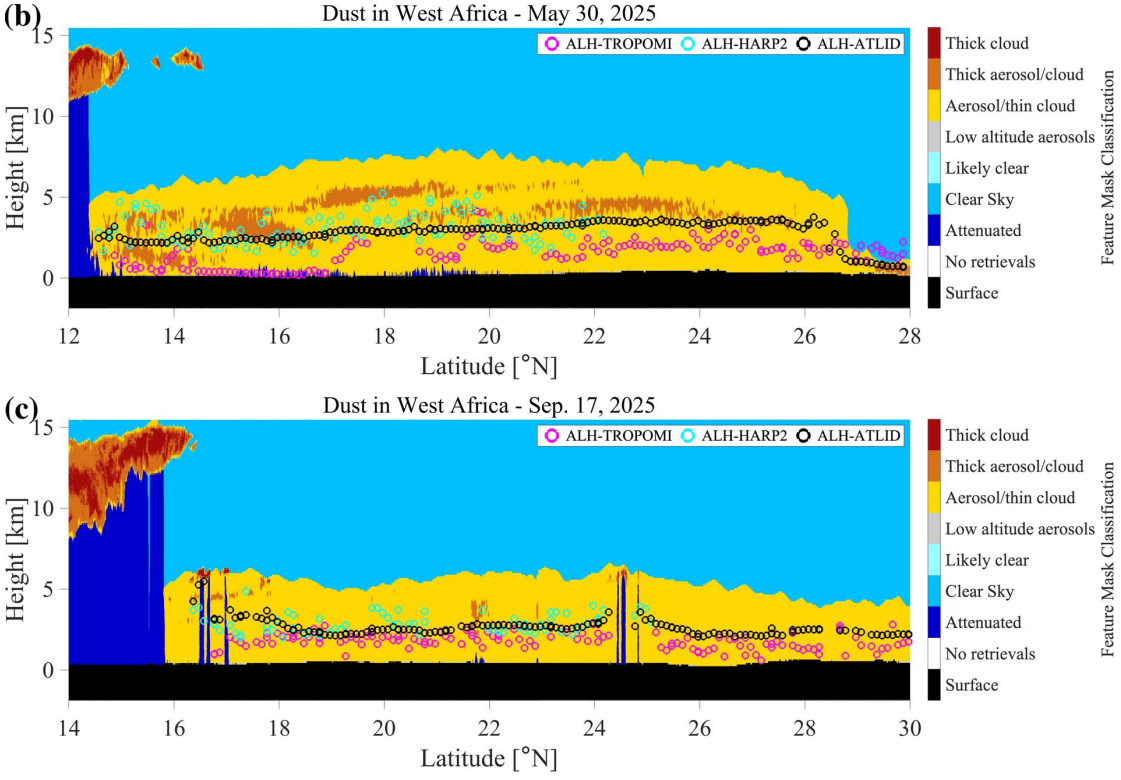

585 **Fig. 11. Comparison of ALH-HARP2 and ALH-TROPOMI with the corresponding ATLID measurements for dust cases on the feature classification curtain plot. Panels (a)-(c) present comparisons of ALH-HARP2 and ALH-TROPOMI with ATLID in three dust cases, respectively.**

5.2.3 West African Dust Transport Event on September 17, 2025

This case occurred during the late summer to early autumn period, when dust activity over the Sahara remains active and 590 atmospheric circulation conditions are favourable for the formation of large-scale SAL transport events. As shown in Fig. 10(g), the true-colour imagery reveals extensive dust transport over the Sahara. The HARP2 retrieval results (Fig. 10(h)) identify elevated ALH in multiple regions, with some areas reaching approximately 4–6 km. However, the spatial distribution of these high-ALH regions (e.g., around $[10°W, 15°N]$ and $[15°W, 28°N]$) is not fully consistent with the TROPOMI retrievals (Fig. 10(i)).

595 To further investigate this discrepancy, vertical velocity fields from NCEP–NCAR reanalysis are used for cross-validation. The mid-tropospheric vertical motion (Fig. 12) indicates a clear structure of ascending and descending air masses. Specifically, at 12:00 UTC on September 17, 2025 (Fig. 12(a)), a region of positive vertical velocity (ω) — indicating subsidence — is observed over the southwestern part of the study area (approximately $-15 - 10°W$). By 18:00 UTC (Fig. 12(b)), this same region transitions to negative ω, indicating a shift from subsidence to upward motion. This transition is 600 likely associated with the interaction between the moist, cooler monsoon flow from the Gulf of Guinea and the hot, dry, dust-laden Harmattan winds from the north.

https://doi.org/10.5194/egusphere-2026-3503
Preprint. Discussion started: 25 June 2026

Their convergence near 15°N forms the Intertropical Discontinuity (ITD), generating strong updrafts that lifts dust particles from lower altitudes to higher altitudes, forming the elevated dust layer (4 – 6 km) observed in Fig. 10(h) (Knippertz and Todd, 2012). In another high-value region (approximately $25-30°N$), persistent negative ω from 12:00 to 18:00 UTC indicates continuous upward motion, contributing to the elevated dust layer there. Unlike the ITD-driven mechanism at lower latitudes, this region is influenced by the Canary Current, a cold ocean current that lowers sea surface temperatures. When extremely hot, dust-laden continental air masses move over the cooler ocean surface, a strong and stable low-level temperature inversion forms. While this inversion suppresses vertical motion over the open ocean, the sharp thermal contrast at the coastal boundary (hot land vs. cool ocean) generates a baroclinic-like effect, inducing strong convective uplift near the coastline. This process enables dust particles to be transported above the boundary layer into the free troposphere, reaching altitudes above 4 km.

As shown in Fig. 11(c), ATLID lidar observations indicate that the dust layer is mainly distributed within the altitude range of approximately 2 – 4 km, exhibiting a relatively stable structure along the satellite track. The comparison shows that within the latitude range of $17°N-26°N$, the HARP2 retrieval can reproduce the variation of dust layer height with good agreement. The TROPOMI retrieval shows a slight underestimation of about 0.5 km but still maintains overall consistency with ATLID observations.

Overall, across the three dust cases, both passive remote sensing approaches can capture the general height range of aerosol layers during West African dust transport events and show good agreement with ATLID measurements. In comparison, the HARP2 retrieval demonstrates better continuity in representing height variations along the ATLID track, whereas the TROPOMI product has an advantage in spatial coverage. However, TROPOMI results appear more fragmented in some regions and exhibit localized underestimation in certain areas.

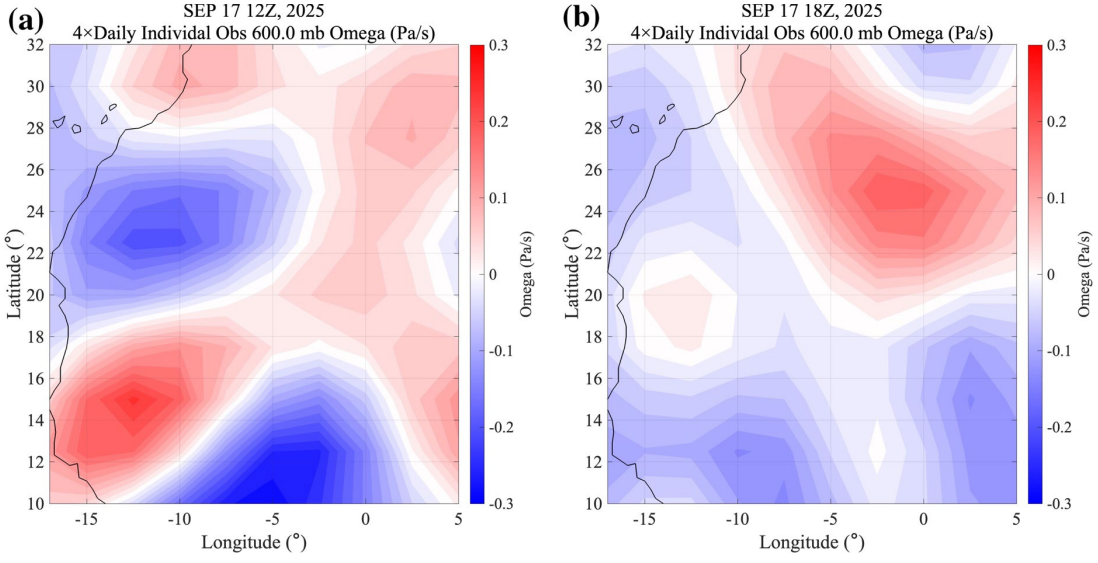

https://doi.org/10.5194/egusphere-2026-3503
Preprint. Discussion started: 25 June 2026

Fig. 12. Spatial distribution of the 700 hPa vertical velocity ω (Pa/s) at 12:00 UTC (left) and 18:00 UTC (right) on 17 September 2025. The data are from the NCEP/NCAR Reanalysis four-times-daily reanalysis dataset provided by the NOAA Physical Sciences Laboratory (https://psl.noaa.gov/mddb2/).

5.3 Validation of ALH Inversion Results

To further quantitatively evaluate the accuracy of ALH retrieved from HARP2 multi-angle polarimetric observations, this study performs point-by-point collocation comparisons with ATLID lidar measurements. ATLID provides aerosol vertical profiles with high vertical resolution and is therefore widely regarded as a reliable reference for validating passive remote sensing retrievals. For quantitative comparison, the ATLID-based aerosol layer height (ALH_{ATLID}) is derived from the Level-2 355 nm extinction coefficient profiles following the method of Koffi et al. (2012), using an extinction-weighted height definition:

$$ALH_{ATLID} = \frac{\sum_{i=1}^{n} \beta_{ext,i} Z_i}{\sum_{i=1}^{n} \beta_{ext,i}} \tag{13}$$

Where $\beta_{ext,i}$ represents the aerosol extinction coefficient (km^{-1}) at altitude Z_i for the i-th vertical layer. The derived ALH_{ATLID} corresponds to the altitude where aerosol extinction is most significant, and its physical meaning is consistent with the quasi-Gaussian vertical distribution assumption adopted in this study (Chen et al., 2021a).

During the collocation process, HARP2 and TROPOMI pixels are first spatially matched with the ATLID ground track, and the data are then aggregated within a 10 km × 10 km window to reduce the impact of spatial scale mismatches. Subsequently, a set of statistical metrics — including Root Mean Square Error (RMSE), Mean Bias (MB), Mean Absolute Error (MAE), correlation coefficient (R), and the proportion of errors within 1 km — is calculated to comprehensively evaluate the retrieval performance. Tables 4 and 5 summarize the statistical error characteristics for each case and under different aerosol types, respectively. Fig. 13 presents the scatterplot comparison based on pixel-level collocation, while Fig. 14 illustrates the error distribution of the matched data pairs.

First, Table 4 presents the statistical comparison between HARP2 and TROPOMI retrievals and ATLID observations for the six selected cases. For the three smoke cases, the RMSE of HARP2 retrievals is 1.25 km, 1.06 km, and 1.10 km, respectively, which is consistently lower than that of TROPOMI (1.65 km, 1.29 km, and 1.55 km). Meanwhile, the mean bias of HARP2 remains close to zero across all cases, whereas TROPOMI exhibits a systematic negative bias of approximately −1 km in all three cases, indicating a general underestimation of smoke layer height. In terms of the proportion of retrievals with errors smaller than 1 km, HARP2 achieves values of 48.33%, 58.68%, and 50.00% for the three smoke events, respectively, which are significantly higher than those of TROPOMI (24.24%, 40.74%, and 15.71%). These results further demonstrate that HARP2 provides higher retrieval accuracy under smoke conditions. For the three dust cases, the RMSE of HARP2 is 1.09 km, 0.96 km, and 0.75 km, respectively, which is generally lower than the corresponding TROPOMI values of 1.32 km, 1.55 km, and 0.94 km. In addition, HARP2 shows relatively small biases, with slight positive bias observed in some cases, while TROPOMI consistently exhibits a pronounced negative bias across all dust events. In particular, for the dust event on

https://doi.org/10.5194/egusphere-2026-3503
Preprint. Discussion started: 25 June 2026

September 17, 2025, HARP2 achieves an RMSE of only 0.75 km, with the proportion of errors within 1 km reaching 84.51%, demonstrating superior retrieval performance.

Aerosol Type	Date	Method	Number	RMSE (km)	MB (km)	MAE (km)	Percentage (error < 1 km)
Smoke	2025/05/28	HARP2	60	1.25	-0.05	1.05	48.33%
		TROPOMI	66	1.65	-1.27	1.51	24.24%
	2025/05/30	HARP2	121	1.06	-0.48	0.86	58.68%
		TROPOMI	81	1.29	-0.96	1.10	40.74%
	2025/06/01	HARP2	80	1.10	-0.19	0.84	50.00%
		TROPOMI	140	1.55	-1.33	1.39	15.71%
Dust	2025/03/18	HARP2	38	1.09	0.08	0.86	55.26%
		TROPOMI	99	1.32	-0.98	1.10	53.53%
	2025/05/30	HARP2	112	0.96	0.35	0.73	75.00%
		TROPOMI	159	1.55	-1.26	1.44	25.79%
	2025/09/17	HARP2	71	0.75	0.08	0.59	84.51%
		TROPOMI	130	0.94	-0.78	0.81	67.69%

Table 4 Comparison of ALH-HARP2, ALH-TROPOMI and ATLID observations for each case

On the basis of individual case statistics, Table 5 further summarizes the overall retrieval performance across all cases, as well as for smoke and dust events separately. For all cases combined, the HARP2 retrieval achieves an RMSE of 1.03 km, which is notably lower than that of TROPOMI (1.40 km), with a near-zero mean bias (−0.07 km). In contrast, TROPOMI exhibits an overall systematic underestimation of approximately 1 km. For the smoke cases, the RMSE of HARP2 is 1.12 km, compared with 1.51 km for TROPOMI. Meanwhile, TROPOMI shows a pronounced negative bias (−1.26 km) under smoke conditions, further indicating its tendency to underestimate ALH in elevated smoke plumes. For the dust cases, HARP2 achieves an RMSE of 0.92 km, significantly lower than the 1.31 km obtained from TROPOMI. In addition, the mean bias of HARP2 is 0.22 km, close to zero, whereas TROPOMI still exhibits a systematic negative bias of approximately −1 km.

To more intuitively illustrate the relationship between retrieval results and ATLID observations, Fig. 13 presents scatterplots comparing ALH retrieved from HARP2 and TROPOMI against ATLID measurements. Overall, both passive remote sensing retrievals show a positive correlation with ATLID observations; however, they exhibit different characteristics in terms of statistical performance. In general, the HARP2 retrievals are closer to the 1:1 consistency line and exhibit lower dispersion, resulting in a smaller RMSE, which indicates better agreement with ATLID in terms of absolute layer height values. In contrast, TROPOMI retrievals show higher correlation coefficients, suggesting stronger capability in capturing the relative variability and spatial–temporal patterns of ALH. When analysed by aerosol type, the smoke cases show that HARP2

https://doi.org/10.5194/egusphere-2026-3503
Preprint. Discussion started: 25 June 2026

retrievals achieve a good linear correlation with ATLID ($R = 0.75$), while TROPOMI exhibits an even higher correlation ($R = 0.93$). However, TROPOMI also shows a pronounced negative bias (bias = −1.26 km), indicating systematic underestimation of smoke layer height in most conditions, which leads to a relatively larger RMSE. For dust cases, the correlation of both methods decreases to some extent, which may be associated with the non-spherical nature and more complex scattering properties of mineral dust particles.

Aerosol Type	Method	Number	RMSE (km)	MB (km)	*R*
All	HARP2	482	1.03	-0.07	0.68
	TROPOMI	675	1.40	-1.13	0.85
Smoke	HARP2	261	1.12	-0.31	0.75
	TROPOMI	287	1.51	-1.26	0.93
Dust	HARP2	221	0.92	0.22	0.40
	TROPOMI	388	1.31	-1.03	0.42

Table 5 Summary of ALH retrieval comparison across all cases, smoke events, and dust events

Additionally, to analyse the differences between the two retrieval methods and ATLID observations from the perspective of error statistics, Fig. 14 presents histograms of ALH differences relative to ATLID, together with their statistical characteristics. As shown in Fig. 14(a), for all cases, the error distribution of ALH-HARP2 is more concentrated around zero (mean = −0.07 km, median = −0.08 km), indicating good overall consistency with the reference. In contrast, ALH-TROPOMI exhibits a clear negative bias, with the distribution shifted toward negative values and a median significantly below zero. For the smoke cases (Fig. 14(b)), ALH-HARP2 shows a relatively larger dispersion (Std = 1.07 km), which may be attributed to the increased complexity of viewing geometry dependence and the amplification of random errors introduced during multi-source data coupling. Nevertheless, the proposed method does not exhibit a systematic underestimation for high-altitude smoke layers, demonstrating better physical consistency. In comparison, ALH-TROPOMI shows a highly concentrated negative deviation, indicating relatively stable retrieval behaviour under strong absorption constraints, but with a persistent systematic low bias in elevated aerosol conditions. For the dust cases (Fig. 14(c)), both methods perform better than in smoke scenarios, which may be related to differences in the physical and optical properties of the two aerosol types. In general, smoke particles are typically smaller and more nearly spherical, exhibiting stronger polarization scattering signatures in the visible range, which is theoretically more favourable for polarimetric retrieval. In contrast, coarse-mode mineral dust particles are highly non-spherical and exhibit weaker polarization signals, reducing the sensitivity of polarization measurements to coarse dust properties (Kalashnikova et al., 2011). However, dust events often present relatively well-defined layered structures, such as the SAL, where aerosol concentration exhibits a clear vertical gradient. This structural feature facilitates the retrieval of ALH or centroid height. In contrast, smoke aerosols are often associated with multilayer structures or mixing with cloud layers, and their strong absorption further complicates radiative transfer

https://doi.org/10.5194/egusphere-2026-3503
Preprint. Discussion started: 25 June 2026

processes. These factors increase retrieval uncertainty and lead to a relatively larger dispersion in smoke-related retrieval results.

Overall, in the validation against ATLID lidar observations, the ALH retrieved from HARP2 multi-angle polarimetric measurements shows generally good agreement with ATLID observations. For both smoke and dust aerosol cases, the HARP2 retrievals can capture the spatial variability of ALH and exhibit relatively small errors and stable statistical characteristics in most cases. This indicates that multi-angle polarimetric observations contain substantial information content for resolving aerosol vertical structure and have strong potential for ALH retrieval. In contrast, the intercomparison results show that the TROPOMI ALH product exhibits a certain degree of systematic underestimation in some cases, although it remains well correlated with ATLID observations overall. This suggests that the product is robust in capturing the variability of ALH. As an operational global aerosol height product, TROPOMI benefits from its wide swath coverage and stable observational capability, making it valuable for global aerosol monitoring and long-term variability studies. It should be noted that although the HARP2 multi-angle polarimetric approach demonstrates relatively high accuracy in ALH retrieval, the results are still affected by uncertainties in aerosol optical model assumptions, surface reflectance parameterization, and viewing geometry. In complex aerosol environments, these factors may introduce additional uncertainties. Future work could further improve the stability and applicability of ALH retrievals by introducing more refined aerosol optical models, improving surface reflectance parameterizations, and incorporating multi-source satellite observations for joint constraints.

Overall, the two passive remote sensing approaches have complementary strengths. HARP2 multi-angle polarimetric observations provide higher information content and show potential advantages in detailed characterization of aerosol vertical structure, while the TROPOMI product plays an important role in long-term, stable global aerosol monitoring. Together, they can provide more reliable data support for studies of aerosol three-dimensional structure and its climatic impacts.

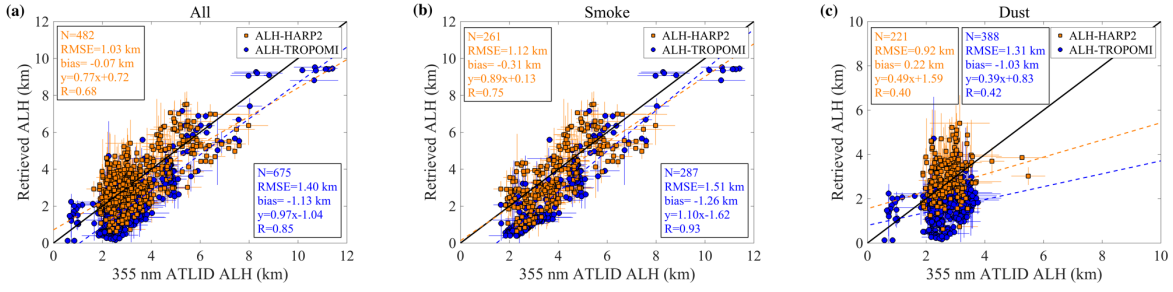

Fig. 13. Comparison of the ALH-HARP2, ALH-TROPOMI with the corresponding ALTID in all cases on a pixel-by-pixel measurement value. (a) Scatter plots of matched ALH-HARP2 (orange markers) and ALH-TROPOMI (blue markers) against ATLID observations, including all matched pixel pairs from all cases. (b) Same as (a), but only including the smoke aerosol cases. (c) Same as (a), but only including the dust cases. The dashed lines in the scatter plots represent the linear regression fits. The one-to-one reference line (black solid line), the number of samples (N), the linear regression equation, and the correlation coefficient (R) are also indicated in the figure. Error bars for both the retrieved ALH and the ATLID-observed ALH represent the standard deviation of values aggregated within a 10 km × 10 km spatial window.

https://doi.org/10.5194/egusphere-2026-3503
Preprint. Discussion started: 25 June 2026

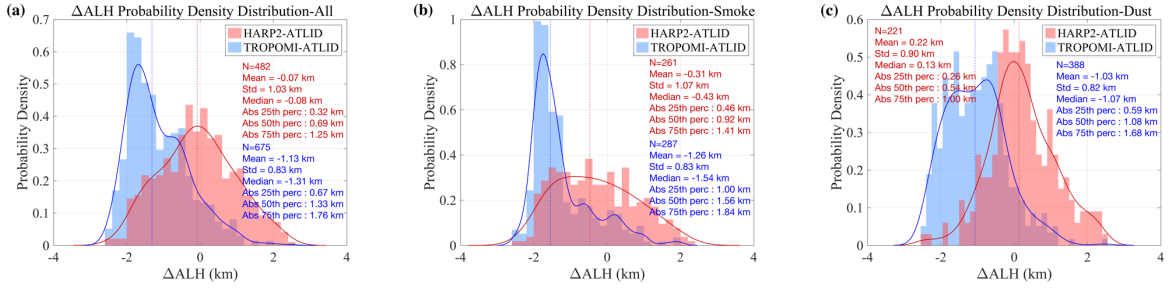

Fig. 14. Histograms and statistical metrics of the differences between ALH-HARP2, ALH-TROPOMI, and ATLID observations at the co-located are presented. The statistics include the total number of data points (N), mean, standard deviation (Std), and median, with the dashed line representing the median value. Panel (a) includes all cases, while Panels (b) and (c) correspond to smoke and dust cases, respectively.

6 Conclusion

This study systematically investigates the information contribution of multi-angle polarimetric observations to aerosol vertical structure retrieval from the perspective of expanding observational information dimensions and develops an ALH retrieval method based on HARP2 multi-angle polarimetric measurements. Through radiative transfer simulations, information content analysis, and typical case studies, the potential advantages of multi-angle polarimetric observations in ALH retrieval are comprehensively evaluated.

First, the response characteristics of TOA Stokes vectors are analysed using radiative transfer simulations, and the observability of ALH is systematically assessed through information content analysis. The results indicate that, compared with single radiance measurements, the introduction of linear polarization components significantly enhances the sensitivity of observations to variations in aerosol vertical distribution. At the 441 nm wavelength, the polarization signal exhibits strong sensitivity to the scattering phase function structure and aerosol particle size characteristics, thereby improving the identifiability of the ALH parameter to some extent. Furthermore, DFS analysis demonstrates that multi-angle polarimetric joint observations can effectively increase the information content of the observation system for ALH. Both the increase in the number of viewing angles and the inclusion of polarization information significantly enhance the degrees of freedom of the retrieval system, thereby providing stronger physical constraints for stable ALH retrieval.

Based on this, this study develops an ALH retrieval method incorporating multi-angle polarimetric observations and validates the method using HARP2 measurements. Six typical cases, including North American wildfire smoke events and West African dust transport events, are selected for analysis. The spatial distributions of the retrieval results are examined and compared with the TROPOMI ALH product and ATLID lidar observations. The case study results show that, for both smoke and dust aerosol scenarios, the HARP2 retrievals can capture the main altitude range of aerosol layers and are generally consistent with ATLID observations over most regions. In high-altitude smoke transport events, HARP2 successfully resolves smoke layers within the 4 – 6 km range, whereas the TROPOMI product exhibits significantly

https://doi.org/10.5194/egusphere-2026-3503
Preprint. Discussion started: 25 June 2026

underestimation in certain regions. For dust events, both methods can identify ALH associated with typical SAL structures, while HARP2 shows better continuity in representing local vertical variations.

Further statistical analysis based on 482 collocated samples indicates that the HARP2 retrievals achieve an RMSE of 1.03 km, significantly lower than the 1.40 km obtained from TROPOMI, with a near-zero mean bias (−0.07 km), demonstrating better overall consistency. For smoke cases, HARP2 yields an RMSE of 1.12 km compared to 1.51 km for TROPOMI, which also exhibits a systematic negative bias of approximately −1.26 km. For dust cases, HARP2 achieves an RMSE of 0.92 km, again outperforming TROPOMI (1.31 km). Scatterplot comparisons and error distribution analyses further indicate that HARP2 retrievals are overall closer to the consistency reference line defined by ATLID, whereas TROPOMI, despite showing relatively high correlation, still exhibits a pronounced negative bias in its retrieval results.

Overall, this study demonstrates that multi-angle polarimetric observations can effectively enhance the physical constraints of ALH retrieval by increasing the dimensionality of observational information. The ALH retrieval method developed based on HARP2 observations shows good accuracy and stability in both smoke and dust aerosol scenarios, providing a promising approach for obtaining aerosol vertical structure information from passive remote sensing. Future work could further improve the stability and applicability of ALH retrieval by refining aerosol optical models, optimizing surface reflectance parameterizations, and integrating multi-source satellite observations for joint retrievals, thereby achieving more robust estimates of ALH.

Author contributions

Pei Li: Writing - review & editing, Writing - original draft, Software, Methodology, Investigation, Formal analysis, Conceptualization. Yong Xue: Writing - review & editing, Supervision, Methodology, Investigation, Conceptualization. Davide Dionisi: Methodology, Conceptualization. Huihui Li: Resources, Data curation. Shuhui Wu: Validation. Xingxing Jiang: Methodology. Botao He: Investigation. Peng Wang: Software, Liying Han: Investigation.

Competing interests

There is no conflict of interest.

Code and data availability

NASA Earth Observing System Data and Information System (EOSDIS) provided VIIRS data (available at https://search.earthdata.nasa.gov/search/). TROPOMI data were available at https://browser.dataspace.copernicus.eu/. The European Space Agency provided EarthCARE (ATLID) L2 Aerosol Profiles data (available at https://explorer.maap.eo.esa.int).

https://doi.org/10.5194/egusphere-2026-3503
Preprint. Discussion started: 25 June 2026

Acknowledgements

This work was supported in part by the National Natural Science Foundation of China (NSFC) under Grant No. 42275147. We acknowledge the public availability of VIIRS data from the NASA Earth Observing System Data and Information System (EOSDIS), the TROPOMI/S5P L2 data from Copernicus Data Space Ecosystem and the EarthCARE data from the European Space Agency. We sincerely thank the anonymous reviewers and the editor for their insightful comments and thoughtful suggestions, which greatly contributed to the improvement of this work.

References

Chen, X., Wang, J., Xu, X., Zhou, M., Zhang, H., Castro Garcia, L., Colarco, P.R., Janz, S.J., Yorks, J., McGill, M., Reid, J.S., de Graaf, M., Kondragunta, S., 2021a. First retrieval of absorbing aerosol height over dark target using TROPOMI oxygen B band: Algorithm development and application for surface particulate matter estimates. Remote Sensing of Environment 265, 112674. https://doi.org/10.1016/j.rse.2021.112674

Chen, X., Xu, X., Wang, J., Diner, D.J., 2021b. Can multi-angular polarimetric measurements in the oxygen-A and B bands improve the retrieval of aerosol vertical distribution? Journal of Quantitative Spectroscopy and Radiative Transfer 270, 107679. https://doi.org/10.1016/j.jqsrt.2021.107679

Choi, W., Lee, H., Kim, J., Park, J., 2021. First TROPOMI Retrieval of Aerosol Effective Height Using O_4 Absorption Band at 477 nm and Aerosol Classification. IEEE Transactions on Geoscience and Remote Sensing 59, 9873–9886. https://doi.org/10.1109/TGRS.2020.3044050

Cohen, J.B., Ng, D.H.L., Lim, A.W.L., Chua, X.R., 2018. Vertical distribution of aerosols over the Maritime Continent during El Niño. Atmospheric Chemistry and Physics 18, 7095–7108. https://doi.org/10.5194/acp-18-7095-2018

Diner, D.J., Nelson, D.L., Chen, Y., Kahn, R.A., Logan, J., Leung, F.-Y., Martin, M.V., 2008. Quantitative studies of wildfire smoke injection heights with the Terra Multi-angle Imaging SpectroRadiometer, in: Remote Sensing of Fire: Science and Application. Presented at the Remote Sensing of Fire: Science and Application, SPIE, pp. 56–64. https://doi.org/10.1117/12.795215

Ding, S., Wang, J., Xu, X., 2016. Polarimetric remote sensing in oxygen A and B bands: sensitivity study and information content analysis for vertical profile of aerosols. Atmospheric Measurement Techniques 9, 2077–2092. https://doi.org/10.5194/amt-9-2077-2016

Doherty, O.M., Riemer, N., Hameed, S., 2008. Saharan mineral dust transport into the Caribbean: Observed atmospheric controls and trends. Journal of Geophysical Research: Atmospheres 113. https://doi.org/10.1029/2007JD009171

Dubovik, O., Herman, M., Holdak, A., Lapyonok, T., Tanré, D., Deuzé, J.L., Ducos, F., Sinyuk, A., Lopatin, A., 2011. Statistically optimized inversion algorithm for enhanced retrieval of aerosol properties from spectral multi-angle polarimetric satellite observations. Atmospheric Measurement Techniques 4, 975–1018. https://doi.org/10.5194/amt-4-975-2011

https://doi.org/10.5194/egusphere-2026-3503
Preprint. Discussion started: 25 June 2026

Dubovik, O., King, M.D., 2000. A flexible inversion algorithm for retrieval of aerosol optical properties from Sun and sky radiance measurements. Journal of Geophysical Research: Atmospheres 105, 20673–20696. https://doi.org/10.1029/2000JD900282

Dubovik, O., Li, Z., Mishchenko, M.I., Tanré, D., Karol, Y., Bojkov, B., Cairns, B., Diner, D.J., Espinosa, W.R., Goloub, P., Gu, X., Hasekamp, O., Hong, J., Hou, W., Knobelspiesse, K.D., Landgraf, J., Li, L., Litvinov, P., Liu, Y., Lopatin, A., Marbach, T., Maring, H., Martins, V., Meijer, Y., Milinevsky, G., Mukai, S., Parol, F., Qiao, Y., Remer, L., Rietjens, J., Sano, I., Stammes, P., Stamnes, S., Sun, X., Tabary, P., Travis, L.D., Waquet, F., Xu, F., Yan, C., Yin, D., 2019. Polarimetric remote sensing of atmospheric aerosols: Instruments, methodologies, results, and perspectives. Journal of Quantitative Spectroscopy and Radiative Transfer 224, 474–511. https://doi.org/10.1016/j.jqsrt.2018.11.024

Dubovik, O., Sinyuk, A., Lapyonok, T., Holben, B.N., Mishchenko, M., Yang, P., Eck, T.F., Volten, H., Muñoz, O., Veihelmann, B., van der Zande, W.J., Leon, J.-F., Sorokin, M., Slutsker, I., 2006. Application of spheroid models to account for aerosol particle nonsphericity in remote sensing of desert dust. Journal of Geophysical Research: Atmospheres 111. https://doi.org/10.1029/2005JD006619

European Space Agency, 2021. TROPOMI Level 2 Aerosol Layer Height (mid-level pressure). https://doi.org/10.5270/S5P-7g4iapn

Fromm, M., Lindsey, D.T., Servranckx, R., Yue, G., Trickl, T., Sica, R., Doucet, P., Godin-Beekmann, S., 2010. The Untold Story of Pyrocumulonimbus. Bulletin of the American Meteorological Society 91, 1193–1210. https://doi.org/10.1175/2010BAMS3004.1

Gandham, H., Dasari, H.P., Karumuri, A., Ravuri, P.M.K., Hoteit, I., 2022. Three-dimensional structure and transport pathways of dust aerosols over West Asia. npj Climate and Atmospheric Science 5, 45. https://doi.org/10.1038/s41612-022-00266-2

Gao, M., Franz, B.A., Zhai, P.-W., Knobelspiesse, K., Sayer, A.M., Xu, X., Martins, J.V., Cairns, B., Castellanos, P., Fu, G., Hannadige, N., Hasekamp, O., Hu, Y., Ibrahim, A., Patt, F., Puthukkudy, A., Werdell, P.J., 2023. Simultaneous retrieval of aerosol and ocean properties from PACE HARP2 with uncertainty assessment using cascading neural network radiative transfer models. Atmospheric Measurement Techniques 16, 5863–5881. https://doi.org/10.5194/amt-16-5863-2023

Graaf, M., Sneep, M., ter Linden, M., Tilstra, L.G., Donovan, D.P., van Zadelhoff, G.-J., Veefkind, J.P., 2025. Improvements in aerosol layer height retrievals from TROPOMI oxygen A-band measurements by surface albedo fitting in optimal estimation. Atmospheric Measurement Techniques 18, 2553–2571. https://doi.org/10.5194/amt-18-2553-2025

Gu, H., Zhang, Y., Fan, C., Li, Z., Hou, W., Liu, Z., Xie, Y., Xu, H., Zhang, L., Ma, J., 2022. A Comprehensive Analysis of Ultraviolet Remote Sensing for Aerosol Layer Height Retrieval from Multi-Angle Polarization Satellite Measurements. Remote Sensing 14, 6258. https://doi.org/10.3390/rs14246258

Hasekamp, O.P., Landgraf, J., 2007. Retrieval of aerosol properties over land surfaces: capabilities of multiple-viewing-angle intensity and polarization measurements. Appl. Opt., AO 46, 3332–3344. https://doi.org/10.1364/AO.46.003332

https://doi.org/10.5194/egusphere-2026-3503
Preprint. Discussion started: 25 June 2026

Hou, W., Li, Z., Wang, J., Xu, X., Goloub, P., Qie, L., 2018. Improving Remote Sensing of Aerosol Microphysical Properties by Near-Infrared Polarimetric Measurements Over Vegetated Land: Information Content Analysis. Journal of Geophysical Research: Atmospheres 123, 2215–2243. https://doi.org/10.1002/2017JD027388

Hsu, N.C., Jeong, M.-J., Bettenhausen, C., Sayer, A.M., Hansell, R., Seftor, C.S., Huang, J., Tsay, S.-C., 2013. Enhanced Deep Blue aerosol retrieval algorithm: The second generation. Journal of Geophysical Research: Atmospheres 118, 9296–9315. https://doi.org/10.1002/jgrd.50712

Illingworth, A.J., Barker, H.W., Beljaars, A., Ceccaldi, M., Chepfer, H., Clerbaux, N., Cole, J., Delanoë, J., Domenech, C., Donovan, D.P., Fukuda, S., Hirakata, M., Hogan, R.J., Huenerbein, A., Kollias, P., Kubota, T., Nakajima, T., Nakajima, T.Y., Nishizawa, T., Ohno, Y., Okamoto, H., Oki, R., Sato, K., Satoh, M., Shephard, M.W., Velázquez-Blázquez, A., Wandinger, U., Wehr, T., Zadelhoff, G.-J. van, 2015. The EarthCARE Satellite: The Next Step Forward in Global Measurements of Clouds, Aerosols, Precipitation, and Radiation. Bulletin of the American Meteorological Society 96, 1311–1332. https://doi.org/10.1175/BAMS-D-12-00227.1

Jeong, M., Hsu, N.C., 2008. Retrievals of aerosol single-scattering albedo and effective aerosol layer height for biomass-burning smoke: Synergy derived from "A-Train" sensors. Geophysical Research Letters 35, 2008GL036279. https://doi.org/10.1029/2008GL036279

Kahn, R.A., Chen, Y., Nelson, D.L., Leung, F., Li, Q., Diner, D.J., Logan, J.A., 2008. Wildfire smoke injection heights: Two perspectives from space. Geophysical Research Letters 35, 2007GL032165. https://doi.org/10.1029/2007GL032165

Kalashnikova, O.V., Garay, M.J., Davis, A.B., Diner, D.J., Martonchik, J.V., 2011. Sensitivity of multi-angle photo-polarimetry to vertical layering and mixing of absorbing aerosols: Quantifying measurement uncertainties. Journal of Quantitative Spectroscopy and Radiative Transfer, Polarimetric Detection, Characterization, and Remote Sensing 112, 2149–2163. https://doi.org/10.1016/j.jqsrt.2011.05.010

Knippertz, P., Todd, M.C., 2012. Mineral dust aerosols over the Sahara: Meteorological controls on emission and transport and implications for modeling. Reviews of Geophysics 50. https://doi.org/10.1029/2011RG000362

Koffi, B., Schulz, M., Bréon, F.-M., Griesfeller, J., Winker, D., Balkanski, Y., Bauer, S., Berntsen, T., Chin, M., Collins, W.D., Dentener, F., Diehl, T., Easter, R., Ghan, S., Ginoux, P., Gong, S., Horowitz, L.W., Iversen, T., Kirkevåg, A., Koch, D., Krol, M., Myhre, G., Stier, P., Takemura, T., 2012. Application of the CALIOP layer product to evaluate the vertical distribution of aerosols estimated by global models: AeroCom phase I results. Journal of Geophysical Research: Atmospheres 117. https://doi.org/10.1029/2011JD016858

Kokhanovsky, A.A., Davis, A.B., Cairns, B., Dubovik, O., Hasekamp, O.P., Sano, I., Mukai, S., Rozanov, V.V., Litvinov, P., Lapyonok, T., Kolomiets, I.S., Oberemok, Y.A., Savenkov, S., Martin, W., Wasilewski, A., Di Noia, A., Stap, F.A., Rietjens, J., Xu, F., Natraj, V., Duan, M., Cheng, T., Munro, R., 2015. Space-based remote sensing of atmospheric aerosols: The multi-angle spectro-polarimetric frontier. Earth-Science Reviews 145, 85–116. https://doi.org/10.1016/j.earscirev.2015.01.012

https://doi.org/10.5194/egusphere-2026-3503
Preprint. Discussion started: 25 June 2026

Lee, J., Hsu, N.C., Bettenhausen, C., Sayer, A.M., Seftor, C.J., Jeong, M.-J., 2015. Retrieving the height of smoke and dust aerosols by synergistic use of VIIRS, OMPS, and CALIOP observations. Journal of Geophysical Research: Atmospheres 120, 8372–8388. https://doi.org/10.1002/2015JD023567

Li, P., Xue, Y., Dionisi, D., He, B., Wang, P., Li, H., 2025. Detecting the layer height of smoke and dust aerosols over land and ocean using ultraviolet dual-wavelength measurements. Remote Sensing of Environment 331, 115001. https://doi.org/10.1016/j.rse.2025.115001

Li, P., Xue, Y., Li, H., He, B., Yin, W., Wang, P., 2024. Three-dimensional reconstruction of aerosols based on spectral radiance matching. Atmospheric Environment 326, 120485. https://doi.org/10.1016/j.atmosenv.2024.120485

Li, Z., Hou, W., Hong, J., Zheng, F., Luo, D., Wang, J., Gu, X., Qiao, Y., 2018. Directional Polarimetric Camera (DPC): Monitoring aerosol spectral optical properties over land from satellite observation. Journal of Quantitative Spectroscopy and Radiative Transfer 218, 21–37. https://doi.org/10.1016/j.jqsrt.2018.07.003

Litvinov, P., Hasekamp, O., Cairns, B., 2011. Models for surface reflection of radiance and polarized radiance: Comparison with airborne multi-angle photopolarimetric measurements and implications for modeling top-of-atmosphere measurements. Remote Sensing of Environment 115, 781–792. https://doi.org/10.1016/j.rse.2010.11.005

Liu, D., Chen, S., Cheng, C., Barker, H.W., Dong, C., Ke, J., Wang, S., Zheng, Z., 2019. Analysis of global three-dimensional aerosol structure with spectral radiance matching. Atmos. Meas. Tech. 12, 6541–6556. https://doi.org/10.5194/amt-12-6541-2019

Maignan, F., Bréon, F.-M., Fédèle, E., Bouvier, M., 2009. Polarized reflectances of natural surfaces: Spaceborne measurements and analytical modeling. Remote Sensing of Environment 113, 2642–2650. https://doi.org/10.1016/j.rse.2009.07.022

Mishchenko, M.I., Cairns, B., Kopp, G., Schueler, C.F., Fafaul, B.A., Hansen, J.E., Hooker, R.J., Itchkawich, T., Maring, H.B., Travis, L.D., 2007. Accurate Monitoring of Terrestrial Aerosols and Total Solar Irradiance: Introducing the Glory Mission. Bulletin of the American Meteorological Society 88, 677–692. https://doi.org/10.1175/BAMS-88-5-677

Nanda, S., de Graaf, M., Veefkind, J.P., Sneep, M., ter Linden, M., Sun, J., Levelt, P.F., 2020. A first comparison of TROPOMI aerosol layer height (ALH) to CALIOP data. Atmospheric Measurement Techniques 13, 3043–3059. https://doi.org/10.5194/amt-13-3043-2020

Nanda, S., de Graaf, M., Veefkind, J.P., ter Linden, M., Sneep, M., de Haan, J., Levelt, P.F., 2019. A neural network radiative transfer model approach applied to the Tropospheric Monitoring Instrument aerosol height algorithm. Atmospheric Measurement Techniques 12, 6619–6634. https://doi.org/10.5194/amt-12-6619-2019

NASA VIIRS Atmosphere Science Team, S., 2023. VIIRS/SNPP Deep Blue Aerosol L2 6-Min Swath 6 km (NRT). https://doi.org/10.5067/VIIRS/AERDB_L2_VIIRS_SNPP_NRT.002

Nelson, D.M., Hu, F.S., Scholes, D.R., Joshi, N., Pearson, A., 2008. Using SPIRAL (Single Pollen Isotope Ratio AnaLysis) to estimate C3- and C4-grass abundance in the paleorecord. Earth and Planetary Science Letters 269, 11–16. https://doi.org/10.1016/j.epsl.2008.03.001

https://doi.org/10.5194/egusphere-2026-3503
Preprint. Discussion started: 25 June 2026

Nishizawa, T., Kudo, R., Oikawa, E., Higurashi, A., Jin, Y., Sugimoto, N., Sato, K., Okamoto, H., 2026. Algorithms to retrieve aerosol optical properties using lidar measurements on board the EarthCARE satellite. Atmospheric Measurement Techniques 19, 729–744. https://doi.org/10.5194/amt-19-729-2026

Parajuli, S.P., Stenchikov, G.L., Ukhov, A., Shevchenko, I., Dubovik, O., Lopatin, A., 2020. Aerosol vertical distribution and interactions with land/sea breezes over the eastern coast of the Red Sea from lidar data and high-resolution WRF-Chem simulations. Atmospheric Chemistry and Physics 20, 16089–16116. https://doi.org/10.5194/acp-20-16089-2020

Peterson, D.A., Campbell, J.R., Hyer, E.J., Fromm, M.D., Kablick, G.P., Cossuth, J.H., DeLand, M.T., 2018. Wildfire-driven thunderstorms cause a volcano-like stratospheric injection of smoke. npj Climate and Atmospheric Science 1, 30. https://doi.org/10.1038/s41612-018-0039-3

Pierangelo, C., Chédin, A., Heilliette, S., Jacquinet-Husson, N., Armante, R., 2004. Dust altitude and infrared optical depth from AIRS. Atmospheric Chemistry and Physics 4, 1813–1822. https://doi.org/10.5194/acp-4-1813-2004

Prospero, J.M., Collard, F.-X., Molinié, J., Jeannot, A., 2014. Characterizing the annual cycle of African dust transport to the Caribbean Basin and South America and its impact on the environment and air quality. Global Biogeochemical Cycles 28, 757–773. https://doi.org/10.1002/2013GB004802

Sanders, A.F.J., de Haan, J.F., Sneep, M., Apituley, A., Stammes, P., Vieitez, M.O., Tilstra, L.G., Tuinder, O.N.E., Koning, C.E., Veefkind, J.P., 2015. Evaluation of the operational Aerosol Layer Height retrieval algorithm for Sentinel-5 Precursor: application to O_2 A band observations from GOME-2A. Atmospheric Measurement Techniques 8, 4947–4977. https://doi.org/10.5194/amt-8-4947-2015

Savtchenko, A., Kummerer, R., Smith, P., Gopalan, A., Kempler, S., Leptoukh, G., 2008. A-Train Data Depot: Bringing Atmospheric Measurements Together. IEEE Transactions on Geoscience and Remote Sensing 46, 2788–2795. https://doi.org/10.1109/TGRS.2008.917600

Sayer, A.M., Hsu, N.C., Bettenhausen, C., Ahmad, Z., Holben, B.N., Smirnov, A., Thomas, G.E., Zhang, J., 2012. SeaWiFS Ocean Aerosol Retrieval (SOAR): Algorithm, validation, and comparison with other data sets. Journal of Geophysical Research: Atmospheres 117. https://doi.org/10.1029/2011JD016599

Sienkiewicz, N., Martins, J.V., McBride, B.A., Xu, X., Puthukkudy, A., Smith, R., Fernandez-Borda, R., 2025. HARP2 pre-launch calibration: dealing with polarization effects of a wide field of view. Atmospheric Measurement Techniques 18, 2447–2462. https://doi.org/10.5194/amt-18-2447-2025

Sokolik, I.N., 2002. The spectral radiative signature of wind-blown mineral dust: Implications for remote sensing in the thermal IR region. Geophysical Research Letters 29, 7-1-7–4. https://doi.org/10.1029/2002GL015910

Spurr, R.J.D., VLIDORT: A linearized pseudo-spherical vector discrete ordinate radiative transfer code for forward model and retrieval studies in multilayer multiple scattering media. Journal of Quantitative Spectroscopy and Radiative Transfer, Volume 102, Issue 2, November 2006, Pages 316-342. https://doi.org/10.1016/j.jqsrt.2006.05.005.

https://doi.org/10.5194/egusphere-2026-3503
Preprint. Discussion started: 25 June 2026

Spurr, R., Christi, M., 2014. On the generation of atmospheric property Jacobians from the (V)LIDORT linearized radiative transfer models. Journal of Quantitative Spectroscopy and Radiative Transfer 142, 109–115. https://doi.org/10.1016/j.jqsrt.2014.03.011

Torres, O., Bhartia, P.K., Herman, J.R., Ahmad, Z., Gleason, J., 1998. Derivation of aerosol properties from satellite measurements of backscattered ultraviolet radiation: Theoretical basis. Journal of Geophysical Research: Atmospheres 103, 17099–17110. https://doi.org/10.1029/98JD00900

Torres, O., Bhartia, P.K., Herman, J.R., Sinyuk, A., Ginoux, P., Holben, B., 2002. A Long-Term Record of Aerosol Optical Depth from TOMS Observations and Comparison to AERONET Measurements. Journal of the Atmospheric Sciences 59, 398–413. https://doi.org/10.1175/1520-0469(2002)059%253C0398:ALTROA%253E2.0.CO;2

van Zadelhoff, G.-J., Donovan, D.P., Wang, P., 2023. Detection of aerosol and cloud features for the EarthCARE atmospheric lidar (ATLID): the ATLID FeatureMask (A-FM) product. Atmospheric Measurement Techniques 16, 3631–3651. https://doi.org/10.5194/amt-16-3631-2023

Wang, J., Xu, X., Ding, S., Zeng, J., Spurr, R., Liu, X., Chance, K., Mishchenko, M., 2014. A numerical testbed for remote sensing of aerosols, and its demonstration for evaluating retrieval synergy from a geostationary satellite constellation of GEO-CAPE and GOES-R. Journal of Quantitative Spectroscopy and Radiative Transfer, Electromagnetic and Light Scattering by Nonspherical Particles XIV 146, 510–528. https://doi.org/10.1016/j.jqsrt.2014.03.020

Wanner, W., Li, X., Strahler, A.H., 1995. On the derivation of kernels for kernel-driven models of bidirectional reflectance. Journal of Geophysical Research: Atmospheres 100, 21077–21089. https://doi.org/10.1029/95JD02371

Werdell, P.J., Behrenfeld, M.J., Bontempi, P.S., Boss, E., Cairns, B., Davis, G.T., Franz, B.A., Gliese, U.B., Gorman, E.T., Hasekamp, O., Knobelspiesse, K.D., Mannino, A., Martins, J.V., McClain, C.R., Meister, G., Remer, L.A., 2019. The Plankton, Aerosol, Cloud, Ocean Ecosystem Mission: Status, Science, Advances. Bulletin of the American Meteorological Society 100, 1775–1794. https://doi.org/10.1175/BAMS-D-18-0056.1

Winker, D.M., Hunt, W.H., McGill, M.J., 2007. Initial performance assessment of CALIOP. Geophysical Research Letters 34. https://doi.org/10.1029/2007GL030135

Winker, D.M., Pelon, J., Coakley, J.A., Ackerman, S.A., Charlson, R.J., Colarco, P.R., Flamant, P.H., Fu, Q., Hoff, R.M., Kittaka, C., Kubar, T.L., Treut, H.L., McCormick, M.P., Mégie, G., Poole, L.R., Powell, K., Trepte, C.R., Vaughan, M.A., Wielicki, B.A., 2010. THE CALIPSO MISSION: A Global 3D View of Aerosols and Clouds. Bulletin of the American Meteorological Society 91, 1211–1229.

Wu, L., Hasekamp, O., van Diedenhoven, B., Cairns, B., Yorks, J.E., Chowdhary, J., 2016. Passive remote sensing of aerosol layer height using near-UV multiangle polarization measurements. Geophysical Research Letters 43, 8783–8790. https://doi.org/10.1002/2016GL069848

Xu, X., Chen, X., Wang, J., Remer, L.A., 2024. Potential of NASA's Plankton, Aerosol, Cloud, and Ocean Ecosystem (PACE) Satellite Observations in the Oxygen Bands for Determining Aerosol Layer Height over Ocean. Journal of Remote Sensing 4, 0167. https://doi.org/10.34133/remotesensing.0167

https://doi.org/10.5194/egusphere-2026-3503
Preprint. Discussion started: 25 June 2026

Xu, X., Wang, J., 2019. UNL-VRTM, A Testbed for Aerosol Remote Sensing: Model Developments and Applications, in: Kokhanovsky, A. (Ed.), Springer Series in Light Scattering: Volume 4: Light Scattering and Radiative Transfer. Springer International Publishing, Cham, pp. 1–69. https://doi.org/10.1007/978-3-030-20587-4_1

Xu, X., Wang, J., Wang, Y., Zeng, J., Torres, O., Reid, J.S., Miller, S.D., Martins, J.V., Remer, L.A., 2019. Detecting layer height of smoke aerosols over vegetated land and water surfaces via oxygen absorption bands: hourly results from EPIC/DSCOVR in deep space. Atmospheric Measurement Techniques 12, 3269–3288. https://doi.org/10.5194/amt-12-3269-2019

Xu, X., Wang, J., Wang, Y., Zeng, J., Torres, O., Yang, Y., Marshak, A., Reid, J., Miller, S., 2017. Passive remote sensing of altitude and optical depth of dust plumes using the oxygen A and B bands: First results from EPIC/DSCOVR at Lagrange-1 point. Geophysical Research Letters 44, 7544–7554. https://doi.org/10.1002/2017GL073939

Zeng, J., Han, Q., Wang, J., 2008. High-spectral resolution simulation of polarization of skylight: Sensitivity to aerosol vertical profile. Geophys. Res. Lett. 35. https://doi.org/10.1029/2008GL035645

Zeng, Z.-C., Chen, S., Natraj, V., Le, T., Xu, F., Merrelli, A., Crisp, D., Sander, S.P., Yung, Y.L., 2020. Constraining the vertical distribution of coastal dust aerosol using OCO-2 O2 A-band measurements. Remote Sensing of Environment 236, 111494. https://doi.org/10.1016/j.rse.2019.111494

Zeng, Z.-C., Natraj, V., Xu, F., Pongetti, T.J., Shia, R.-L., Kort, E.A., Toon, G.C., Sander, S.P., Yung, Y.L., 2018. Constraining Aerosol Vertical Profile in the Boundary Layer Using Hyperspectral Measurements of Oxygen Absorption. Geophysical Research Letters 45, 10,772-10,780. https://doi.org/10.1029/2018GL079286